sperm nuclei in the cytoplasm which had lipid droplets, Golgi body, and collapsed cristae of mitochondria in the 0.5 µg recipient group The Sertoli cells indicated the phagocytic activity to eliminate abnormal spermatozoa (Fig. 3f). Similar effects were observed in other nano-TiO$_2$ recipient groups.

Discussion

The present study has first demonstrated rutile-type nano-TiO$_2$ in suspensions and in the offspring testis of pregnant mice treated by subcutaneous injection. In the suspension prior to injection, DLS measurement showed that under the most diluted suspension the nano-TiO$_2$ formed small agglomerates as Nanometer sized, 193.3 ± 5.4 nm in average diameter. In the original suspension, they formed large agglomerates as micron sized 1980.3 ± 95.8 nm in average diameter. At the sequentially diluted of 1–1,000 µg/ml suspensions, the agglomerates sizes decreased with diluting concentrations. They were obviously composed of about 35 nm in primary diameter (Figs. 1c). This phenomenon indicated that the increased concentrations led to increase agglomerates of nano-TiO$_2$ in the suspensions.

Furthermore, we observed dose–dependent translocation of nano-TiO$_2$ across the placental barrier and biodistribution in testis in vivo. The electron dense particles found in the offspring seminiferous epithelium of all nano-TiO$_2$ recipient groups were confirmed to be the agglomerates around 200 nm by X-ray spectrometry under SEM and TEM. This analysis directly shows the localized position and number of the agglomerates. This suggested that even at the lowest dose, 0.5 µg of nano-TiO$_2$, it was possible to detect the distribution to the seminiferous epithelium. Regarding semi-quantification, agglomerate deposition in the testicular sections was correlated with nano-TiO$_2$ doses injected into pregnant mice (Fig. 2g). However, only small agglomerates of nano-TiO$_2$ below 200 nm were found in the offspring seminiferous epithelium of all recipient groups, independent from the injected dose during pregnancy. We have found the nano-TiO$_2$ translocation "in vivo" which agrees with the presumption from the experiment with ex vivo human placental perfusion (Wick et al. 2010), where nanomaterials with the diameter up to 240 nm cross the placental barrier. Similarly, rutile-type nano-TiO$_2$ (20.6 nm) retention in mouse lung following intratracheal instillation of 18, 54, and 162 µg/mouse

was investigated using nanoscale hyperspectral microscopy. The hyperspectral mapping showed dose–dependent retention of nano-TiO$_2$ in the lung at up to 28 days post instillation. Several inflammatory mediators were shown to have changed in a dose- and time-dependent manner at both the mRNA and protein levels by DNA microarray analysis (Husain et al. 2013).

Generally, an ICP-MS is used to calculate the mass concentrations of nanoparticles in tissue. After examining the acute toxicity and biodistribution by ICP-MS, nano-TiO$_2$ have been found in the liver, kidneys, spleen, and lungs of adult mice after oral gavage administration of three sizes of anatase nano-TiO$_2$ (25, 80, and fine 155 ± 33 nm, 5 g/kg body weight). The 25 and 80 nm nanosized TiO$_2$ particles were shown to induce significant lesions in the liver and kidneys of female mice (Wang et al. 2007). On the other hand, nano-TiO$_2$ of both anatase and rutile forms (70/30) in the size range 20–30 nm administrated intravenously (at 5 mg/kg body weight) became decreasingly detectable over time in the liver, spleen, kidneys, and lungs of rats. It was concluded that nano-TiO$_2$ could be used safely in low doses due to the lack of any remarkable toxic health effects (Fabian et al. 2008).

The TEM observations reveal the failure of spermiation from Sertoli cells in all recipient groups. This may be caused by the biodistribution of nano-TiO$_2$ in seminiferous epithelium. This result was consistent with the investigations that nanoparticles exposure caused the toxicity on testicular function of totally different experiments (Hemmingsen et al. 2009) and (Kyjovska et al. 2013). Further studies are needed to evaluate biodistribution and effect of nano-TiO$_2$ exposure during pregnancy in more detail.

Conclusion

The average diameter (Z-average) of nano-TiO$_2$ prior to injection was increased in a dose–dependent manner; 1–1,000 µg/ml suspensions were from 193.3 ± 5.4 to 1980.3 ± 95.8 nm in diameter. The biodistribution in the testicular sections examined at 12 weeks postpartum were correlated between nano-TiO$_2$ doses injected to pregnant mice and the number of agglomerates in the testis by semi-quantitative evaluation. However, only small agglomerates of nano-TiO$_2$ below 200 nm transferred to the offspring after crossing the placental barrier, independent from the injected dose during

pregnancy. The failure of spermiation from Sertoli cells and elimination of abnormal spermatozoa were observed in all nano-TiO$_2$ recipient groups.

References

Chen HH, Chien CC, Petibois C, Wang CL, Chu YS, Lai SF, Hua TE, Chen YY, Cai X, Kempson IM, Hwu Y, Margaritondo G (2011) Quantitative analysis of nanoparticle internalization in mammalian cells by high resolution X-ray microscopy. J Nanobiotechnol 9:14–28

De Jong WH, Hagens WI, Krystek P, Burger MC, Sips AJAM, Geertsma RE (2008) Particle size-dependent organ distribution of gold nanoparticles after intravenous administration. Biomaterials 29:1912–1919

Donaldson K, Stone V, Tran CL, Kreyling W, Borm PJA (2004) Nanotoxicology. Occup Environ Med 61:727–728

Fabian E, Landsiedel R, Ma-Hock L, Wiench K, Wohlleben W, van Ravenzwaay B (2008) Tissue distribution and toxicity of intravenously administered titanium dioxide nanoparticles in rats. Arch Toxicol 82(3):151–157

Hemmingsen JG, Hougaard KS, Talsnass C, Wellejus A, Loft S, Wallin H, Moller P (2009) Prenatal exposure to diesel exhaust particles and effect on the male reproductive system in mice. Toxicology 264:61–68

Husain M, Saber AT, Guo C, Jacobsen NR, Jensen KA, Yauk CL, Williams A, Vogel U, Wallin H, Halappanavar S (2013) Pulmonary instillation of low doses of titanium dioxide nanoparticles in mice leads to particle retention and gene expression changes in the absence of inflammation. Toxicol Appl Pharmacol 269(3):250–262

Komatsu T, Tabata M, Kubo-Irie M, Shimizu T, Suzuki K, Nihei Y, Takeda K (2008) The effects of nanoparticles on mouse testis Leydig cells in vitro. Toxicol In Vitro 22:1825–1831

Kyjovska ZO, Boisen AMZ, Jackson P, Wallin H, Vogel U, Hougaard KS (2013) Daily sperm production: application in studies of prenatal exposure to nanoparticles in mice. Reprod Toxicol 36:88–97

Mayhew TM, Muhlfeld C, Vanhecke D, Ochs M (2009) A review of recent methods for efficiently quantifying immunogold and other nanoparticles using TEM sections through cells, tissues and organs. Ann Anat 191:153–170

Maynard AD (2006) Safe handling of nanotechnology. Nature 444:267–269

Nel A, Xia T, Madler L, Li N (2006) Toxic potential of materials at the nanolevel. Science 311:622–627

Oberdorster G, Oberdorster E, Oberdorster J (2005) Nanotoxicology: an emerging discipline evolution from studies of ultrafine particles. Environ Health Perspect 113:823–839

Patri A, Umbreit T, Zheng J, Nagashima K, Goering P, Francke-Carroll S, Gordon E, Weaver J, Miller T, Sadrieh N, McNeil S, Stratmeyer M (2009) Energy dispersive X-ray analysis of titanium dioxide nanoparticle distribution after intravenous and subcutaneous injection in mice. J Appl Toxicol 29:662–672

Sharpe RM, Atanassova N, McKinnell C, Parte P, Turner KJ, Fisher JS, Kerr JB, Groome NP, Macpherson S, Millar MR, Saunders PTK (1998) Abnormalities in functional development of the Sertoli cells in rats treated neonatally with diethylstilbestrol: a possible role for estrogens in Sertoli cell development. Biol Reprod 59:1084–1094

Soto KF, Carrasco A, Powell TG, Garza KM, Murr LE (2005) Comparative in vitro cytotoxicity assessment of some manufactured nanoparticulate materials characterized by transmission electron microscopy. J Nanopart Res 7(2–3):145–169

Takeda K, Suzuki K, Ishihara A, Kubo-Irie M, Fujimoto R, Tabata M, Oshio S, Nihei Y, Ihara T, Sugamata M (2009) Nanoparticles transferred from pregnant mice to their offspring can damage the genital and cranial nerve systems. J Health Sci 55(1):95–102

Umbreit TH, Francke-Carroll S, Weaver JL, Miller TJ, Goering PL, Sadrieh N, Stratmeyer ME (2011) Tissue distribution and histopathological effects of titanium dioxide nanoparticles after intravenous or subcutaneous injection in mice. J Appl Toxicol 32:350–357

Wang J, Zhou G, Chen C, Yu H, Wang T, Ma Y, Jia G, Gao Y, Li B, Sun J, Li Y, Jiao F, Zhao Y, Chai Z (2007) Acute toxicity and biodistribution of different sized titanium dioxide particles in mice after oral administration. Toxicol Lett 168(2):176–185

Warheit DB, Sayes CM, Reed KLS, Swain KA (2008) Health effects related to nanoparticles exposures: environmental, health and safety considerations for assessing hazards and risks. Pharmacol Ther 120:35–42

Wick P, Malek A, Manser P, Meili D, Maeder-Althaus X, Diener L, Diener P-A, Zisch A, Krug H, Mandach U (2010) Barrier capacity of human placenta for nanosized materials. Environ Health Perspect 118:432–436

Yamashita K, Yoshioka Y, Higashisaka K, Mimura K, Morishita Y, Nozaki M, Yoshida T, Ogura T, Nabeshi H, Nagano H, Abe Y, Kamada H, Monobe Y, Imazawa T, Aoshima H, Shishido K, Kawai Y, Mayumi T, Tsunoda S, Itoh N, Yoshikawa T, Yanagihara I, Saito S, Tsutsumi Y (2011) Silica and titanium dioxide nanoparticles cause pregnancy complications in mice. Nat Nanotechnol 6(5):321–328

Yang H, Liu C, Yang D, Zhang H, Xi Z (2009) Comparative study of cytotoxicity, oxidative stress and genotoxicity induced by four typical nanomaterials: the role of particle size, shape and composition. J Appl Toxicol 29(1):69–78

Yoshida S, Hiyoshi K, Oshio S, Takano H, Takeda K (2010) Effect of fetal exposure to carbon nanoparticles on reproductive function in male offspring. Fertil Steril 93(5):1695–1699

Tunable plasma lipoprotein uptake/transport across the blood–brain barrier[☆]

Kenichiro Suzuki [a,b,*], Denis Adigüzel [b], Takanori Shinotsuka [a], Rei Ishibashi [a], Izumi Eguchi [a],
Hideaki Oshima [a], Retsu Taniguchi [a], Stefan Thalhammer [b], Ken Takeda [a]

[a] Research Institute for Science & Technology, Tokyo University of Science, Chiba 278-8510, Japan
[b] Institute of Radiation Protection, Helmholtz Zentrum München, Neuherberg 85764, Germany

HIGHLIGHTS

- Biotechnological tools such as biocompatible nanoparticles have promising potential for theranostic strategies.
- Our study demonstrates the application of specifically constructed nanoparticles in the form of tunable plasma lipoproteins.
- Tuning of phosphatidylcholines and apolipoprotein B100 on nanoparticle surfaces is especially helpful for delivery route of glial precursor cells.

GRAPHICAL ABSTRACT
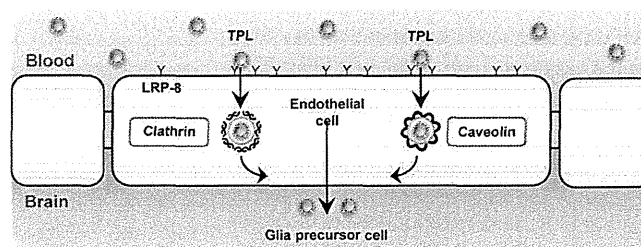
ABSTRACT

Brain development and maintenance requires transportation of cerebral sustenance across the blood–brain barrier. Disorders of this process can induce neurodegenerative diseases, which can affect numerous patients and incur significant treatment expenses. Recent scientific advances suggest that knowledge of this transportation will lead to the development of tailor-made theranostic strategies. Biotechnological tools such as biocompatible nanoparticles have promising potential in this context, however, information about their consequences in the brain is largely unknown. The present study demonstrates the application of specifically constructed cerebral sustenance nanoparticles in the form of tunable plasma lipoproteins to provide information about their pathways to the brain and delivery to glia cells. Individual cell analysis in brain sections enabled us to understand the accumulation of tunable plasma lipoproteins in the cerebral cortex, striatum, and cerebellum, which have been previously identified as the incident regions of Alzheimer's disease, Parkinson's disease, and spinocerebellar ataxia. The adjustability of the tunable plasma lipoproteins enables their use in theranostic applications against neurodegenerative diseases.

© 2013 The Authors. Published by Elsevier B.V. All rights reserved.

* Corresponding author at: Research Institute for Science & Technology, Tokyo University of Science, 2641 Yamazaki, Noda-shi, Chiba 278-8510, Japan.
Tel.: +81 4 7124 1501.
E-mail addresses: k_suzuki@rs.noda.tus.ac.jp, kenichiro-suzuki@i.softbank.jp (K. Suzuki).

1. Introduction

The brain regulates mental and motor functions, which are based on neural networks. Neural network changes such as synaptogenesis, myelination, and neuro- and glio-genesis are associated with environmental factors and individual life events [1]. These changes are produced and preserved by cerebral sustenance transportation across the blood-brain barrier (BBB) [2]. It is generally known that glial cells such as astrocytes and oligodendrocytes play roles in brain development and maintenance [3]. They are not only relevant to the functions of synaptogenesis, myelination, and BBB, but are also involved in the pathogenesis of Alzheimer's disease (AD), Parkinson's disease (PD), and progressive spinocerebellar ataxia (SCA) [2,3]. In addition, it suggests that AD, PD, and SCA generation are induced by the loss of synapses and myelin or the malfunction of BBB in the brain [2,3]. Glial cells are responsible for the preservation of synapses, myelin, and BBB [2,3]. Therefore, innovation to achieve the aim of delivering drugs to glial cells will lead to key advancements in the development of effective theranostic methods [3,4]. However, the pathway from the plasma to glial cells for delivering drugs is as yet unknown.

Neurodegenerative diseases (NDs) such as AD, PD, and SCA are strongly associated with brain aging. These pathological phenotypes have been found in specific brain regions such as the cerebral cortex (AD), striatum (PD), and cerebellum (SCA) [5,6]. Clinical studies suggest that low vitamin A, D, and E levels in plasma contribute to AD, PD and SCA pathogenesis [5,6]. Since mammals are not able to synthesize essential substances such as fat-soluble vitamin A, D, and E, they must be extracted from their diet in the form of plant carotenes or animal retinyl esters, which are stored as retinoids in the liver following ingestion. These vitamins are subsequently transported by plasma lipoproteins (PLs) from the liver into the cardiovascular system [7,8]. But, incorporation of vitamin A, D, and E into PLs through retinol-binding proteins, vitamin D-binding proteins, and α-tocopherol transfer proteins are impaired in AD, PD, and SCA [5,6]. Moreover, it is widely accepted that vitamin A, D, and E are required for synaptogenesis, myelination, and glio-differentiation [9]. Consequently PLs that carry vitamins across the BBB could be vital for glial cells such as astrocytes and oligodendrocytes.

PL core consists mainly of triglycerides, (esterified) cholesterols, fat-soluble vitamins, fatty acids, and hormones, while the shell is composed of phospholipids, primarily phosphatidylcholines (PCs) and sphingomyelins, and apolipoproteins (Apos), such as Apo-A1-4, Apo-B48, Apo-B100, Apo-C1-3, ApoD, Apo-E2-4, and Apo-J [7,8]. PLs in plasma are found in high-density lipoproteins (HDLs), low-density lipoproteins (LDLs), intermediate-density lipoproteins (IDLs), very low-density lipoproteins (VLDLs), and chylomicrons. LDLs, IDLs, and VLDLs, which carry fat-soluble vitamins, mainly contain Apo-B100 [7,8]. Here, we hypothesize that PCs and Apo-B100 in LDLs would be targetor for glial cells. There is now evidence that glial cells highly express heparan sulfate proteoglycans and chondroitin sulfate proteoglycans, which can bind to LDLs [10,11]. Unfortunately, LDL pathway to glial cells has yet been uncharacterized.

In previous studies of brain delivery system, it has been shown that the modifications of nanoparticle surfaces are common approach to achieve novel drug therapies for delivering nanoparticles to the brain [12–15]. Actually, polysorbate 80 with Apo-B or Apo-E-mediated transport at the BBB has been demonstrated as targets for nanoparticle delivery to the brain [12]. However, it has been suggested that the polysorbate 80 induce toxic affects on the BBB permeability [12]. Therefore, future study for novel modification of nanoparticle surfaces should be focus on. Moreover, gold nanoparticles (AuNPs) are useful for the development of clinical applications and treatment strategies, since AuNPs are intended for practical use as contrast agents for an X-ray computed tomography (CT) [16–18].

Here our study demonstrates the application of specifically constructed cerebral sustenance nanoparticles in the form of tunable plasma lipoproteins (TPLs) in order to brain delivery system specifically targeting a subpopulation of glial cells.

2. Materials and methods

2.1. Preparation and characterization of tunable plasma lipoproteins

AuNPs of 20 nm diameter were produced by the Turkevich method [19] and were diluted to a final concentration of 500 μg/ml. PCs (850325P, Avanti Polar Lipids, USA) were dissolved by vortexing in distilled water (ppb level) to a concentration of 1 mg/ml at 37 °C. Aggregates were removed by filtration through a 100 nm cutoff filter (SLVV033RS, Millipore, USA). A 400 μl aliquot of the resulting solution was added to 100 μl of the AuNPs. The AuNPs were coated with the PCs by stirring overnight at 37 °C. The sizes and shapes of the resulting TPLs were determined via transmission electron microscopy (TEM) (JEM-1200 EXII, JEOL, Japan) with negative staining with uranyl acetates. The cell tracker, CM-DiI (DiI) (C7000, Molecular Probes™, USA), was added at a rate of 0.5 μl per 500 μl of distilled water from a 1 mg/ml stock solution in DMSO. Next, 500 μl of the diluted DiI-solution was mixed with 500 μl of the PC-coated AuNPs by gentle stirring, followed by incubation at 37 °C for 30 min inside a sealed tube. Finally, 1 ml of 1 μg/ml Apo-B100 (A5353, Sigma, USA) in saline was added to 1 ml of the DiI-labeled PC-coated AuNPs and incubated for 3 h at 37 °C. The TPLs were re-dispersed in saline and residual PC, Apo, and DMSO solvent were removed by centrifuging twice at 20,000 × g for 5 min. Remaining aggregates were removed by filtration using a 100 nm cutoff filter. Both their hydrodynamic diameter and their PDI were determined by DLS measurements (Nano-ZS, Sysmex, Netherlands). Particle number data (%) were obtained from distribution analyses of the non-negative linear least squares method.

2.2. In vitro experiments

Endothelial cells (ECs) (bEnd.3, ATCC, USA) from mouse brains were cultured in cell culture medium (DMEM, Wako, Japan), supplemented with 10% heat-inactivated fetal bovine serum (Bio West, France) and 0.1% gentamycin (Sigma–Aldrich, USA). Incubation was carried out at 37 °C in a humidified atmosphere of 5% CO_2. The ECs were seeded to a density of 0.7×10^4 cells/cm^2 onto glass plates (1.1 cm^2) that were coated with rat-tail collagen to a density of 5 μg/cm^2 inside flat bottom 24-well plates (area: 1.55 × 1.55 cm^2, height: 1.75 cm). ECs that grew to sub-confluence, corresponding to final cell densities of 2.5×10^4 cells/cm^2, were treated with TPL for different incubation times (6 and 12 h). 100 μl of TPL were added to 900 μl of the cell medium to achieve a final concentration of 2.5 μg/ml. The TPL-containing cell culture medium was replaced with non-TPL-enriched cell medium 30 min after the end of the 12 h incubation. The ECs were then washed twice with PBS and fixed with 4% paraformaldehyde. For the immunocytochemical analyses, ECs were blocked with 3% goat serum for 20 min and were incubated overnight with primary antibodies to clathrin HC H-300 (sc-9069, Santa Cruz Biotechnology, USA), caveolin-1 (C-term), LRP8, and LDL receptor (C-term) (1249-1, 3156-1, and 1956-1, Epitomics Inc., USA) at 4 °C. They were subsequently incubated with secondary antibodies: Alexa Fluor®

488 goat anti-rabbit IgG (A11034, Molecular probes, USA) and their nuclei were stained using H33342 (B2261, Sigma–Aldrich, USA). Cell imaging was achieved using a confocal microscope (Leica SP-II, Leica, Germany) with a 63× oil immersion objective. Endothelial cell vesicle with internalized TPL was determined via TEM.

2.3. In vivo experiments

100 μl of 12.5 or 250 μg/ml saline-diluted TPLs were tail-vein-injected into C57BL/6J mice. After 24 h they were killed by an intraperitoneal injection of pentobarbital diluted in saline and perfused via the heart with 2–5 ml of 0.01 M PBS and 4% paraformaldehyde. The flow rate was 1 ml/min. The brains were removed and fixed with 4% paraformaldehyde in PBS for 2 days. After dehydration in 5% sucrose, the samples were sectioned to a thickness of 10 μm along the sagittal surfaces using a microtome (LS-113, Yamato, Japan). Serial sections were cut from the interaural side of the mouse brain. For immunohistochemical analyses of the brain, the sections were incubated overnight with the primary rabbit polyclonal anti-Olig2 antibody (AB9610, Millipore, USA) at 4 °C. Subsequently, the sections were incubated with secondary antibodies: Alexa Fluor® 488 chicken anti-rabbit IgG (A21441, Molecular probes, USA). Brain ECs were stained using FITC-conjugated TOMATO lectin (FL-1171, Vector Laboratories, USA). The cell nuclei were stained using H33342. The fluorescent signals from Olig2 and TPLs in the brain sections were analyzed by

fluorescence microscopy (BZ-9000, KEYENCE, Japan) with a Plan Apo 20×/0.75 DIC N2 objective lens.

2.4. Statistical analysis

Statistical significance was determined by Student's t-test (Fig. 2B andSupplementary Fig. 2B) and Tukey's test (Fig. 3C). Differences were considered significant with a P value; $*P<0.005$ by Student's t-test, $* P<0.05$ by Tukey's test.

Supplementary data associated with this article can be found, in the online version, at http://dx.doi.org/10.1016/j.colsurfa.2013.05.053.

3. Results and discussion

3.1. Development of tunable plasma lipoproteins

The structure of PLs and the self-assembly processes of TPLs are depicted in Fig. 1A. The term "tunable" is used to refer to refinement in terms of size and shape, phospholipid and protein coating, or delivery routes. To synthesize the TPLs, AuNPs were used to assemble the TPL cores. AuNPs have negative charges at the hydrophobic surfaces. This AuNP behaves likes a hydrophobic solution, and therefore constitutes an aqueous dispersion of insoluble solid particles [20]. AuNPs were then functionalized with biomolecules containing PCs and Apo-B100, which are common components of LDLs [8]. The synthesis was based on a self-assembly
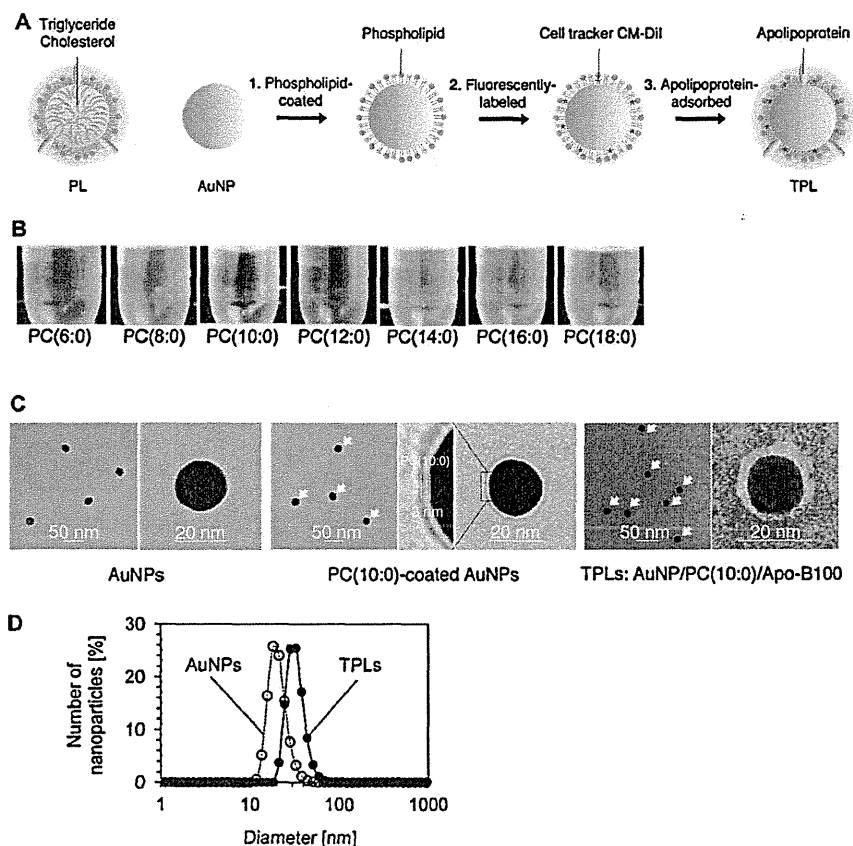

Fig. 1. Preparation and characterization of tunable plasma lipoproteins. (A) The schematic illustration of plasma lipoproteins (PLs) and the schematic depiction of the self-assembly steps involved in the production process of tunable plasma lipoproteins (TPLs). Gold nanoparticles (AuNPs) were (1) coated with phosphatidylcholines (PCs) and (2) labeled with the cell tracker CM-DiI for fluorescent imaging. Finally, (3) apolipoprotein-B100 were added. (B) Images of TPL-solutions produced by PCs with different lengths of saturated fatty acid hydrocarbon chains (6:0, 8:0, 10:0, 12:0, 14:0, 16:0, and 18:0). Red color indicates that TPLs are dispersed in saline. (C) Transmission electron micrographs of AuNPs, PC(10:0)-coated AuNPs, and TPLs: AuNP/PC(10:0)/Apo-B100. Arrows show the PCs (10:0) and Apo-B100. The coated layer is visible as a bright contrast at the particle surface. The PC layer thickness is 3 nm (see a magnified view). (D) Hydrodynamic particle diameters of AuNPs in water and TPLs in saline.
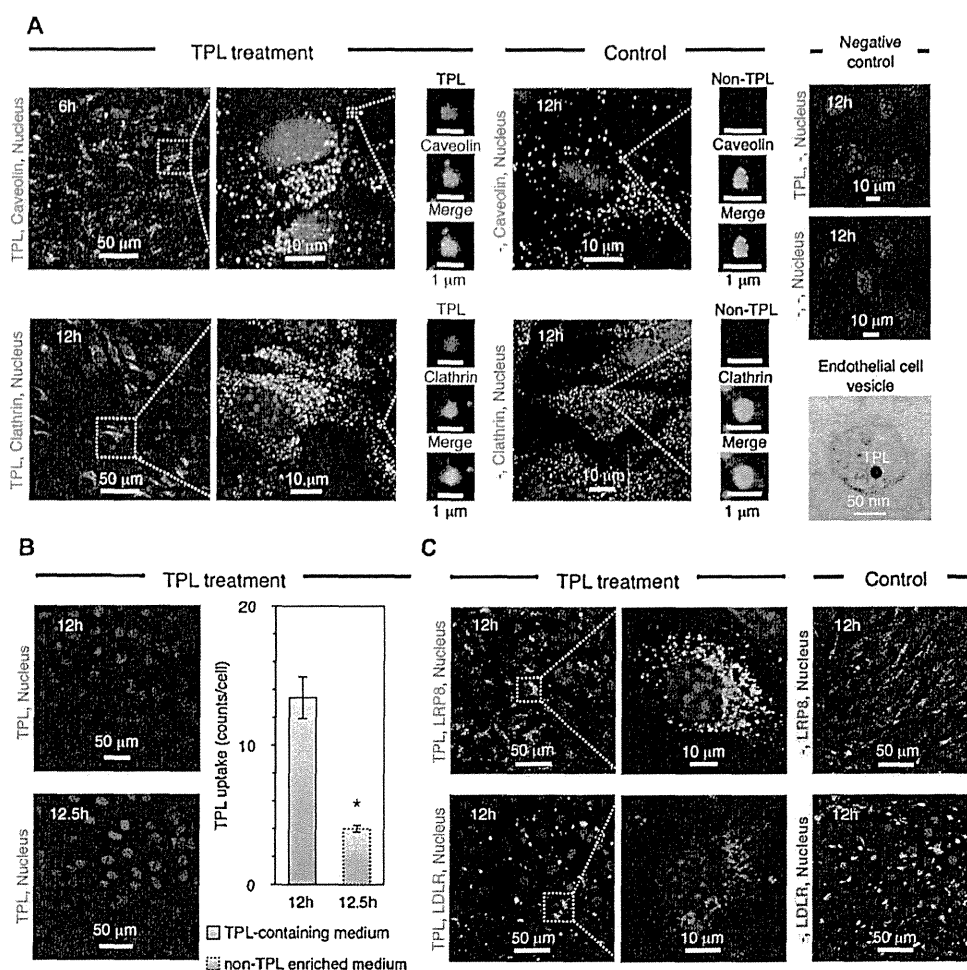
Fig. 2. Analyses of tunable plasma lipoproteins internalized into endothelial cells. (A) Confocal microscopy images of clathrin- and caveolin-coated vesicles in endothelial cells (ECs) incubated with tunable plasma lipoproteins (TPLs) and saline (control). Green ($\lambda_{Ex} = 495$ nm, $\lambda_{Em} = 519$ nm for Alexa Fluor® 488) indicates clathrin and caveolin. Red signals ($\lambda_{Ex} = 553$ nm, $\lambda_{Em} = 570$ nm for cell tracker CM-DiI) correspond to TPLs. The nuclei in the ECs are stained using H33342 (blue color: $\lambda_{Ex} = 355$ nm, $\lambda_{Em} = 465$ nm). Merged color (yellow) indicates that clathrin and caveolin were colocalized with TPLs. Negative controls indicate that green and red signals are not due to background. Transmission electron micrographs of an endothelial cell vesicle with internalized TPL. (B) TPL uptake after replacement of TPL-containing cell culture medium with non-TPL-enriched cell medium after 12 h of incubation. Clearly visible is a decrease in the previously internalized TPL in the EC after 30 min. Estimations of the amount of TPL uptake into ECs were performed by confocal microscopy. Each data point represents the mean ± S.E. of $n = 5$ images (237 μm × 237 μm). *$P < 0.005$ by Student's t-test. (C) Confocal microscopy images of low-density lipoprotein receptor-related protein 8 (LRP8) and low-density lipoprotein receptor (LDLR) in ECs incubated with TPLs. Green ($\lambda_{Ex} = 495$ nm, $\lambda_{Em} = 519$ nm for Alexa Fluor® 488) indicates LRP8 and LDLR. Red signals indicate TPLs. The EC nuclei were stained using H33342.

process. PCs with different lengths of saturated fatty acid hydrocarbon chains (6:0, 8:0, 10:0, 12:0, 14:0, 16:0, and 18:0) were investigated. PCs (10:0 and 12:0) adsorbed solely to AuNP surfaces, which additionally increased their dispersion rate in saline (shown in Fig. 1B). However, PCs (6:0, 8:0, 14:0, 16:0, and 18:0) were insufficiently adsorbed at AuNP surfaces, and PC-uncoated AuNPs were aggregated in saline. This phenomenon can be understood from the solubility (known as critical micelle concentration) of PCs with different lengths of saturated fatty acid hydrocarbon chains (6:0–18:0). By comparison, the PCs (14:0–18:0) were not dispersed in an aqueous solution due to their low solubility. Alternatively, PCs (6:0 and 8:0) were not adsorbed at AuNP surfaces due to their high solubility. This factor contributes to their self-assembly process. As shown in Fig. 1C, AuNPs, PC(10:0)-coated AuNPs, and TPLs: AuNP/PC(10:0)/Apo-B100 were observed by TEM. These results indicate that the AuNP surfaces are coated by PCs (10:0) and Apo-B100. The surface coverage of Apo-B100 adsorbed to the PC(10:0)-coated AuNPs was 96 ± 3.1% ($n = 63$

particle). Dynamic light scattering (DLS) analyses were used to confirm hydrodynamic particle diameter of AuNPs and TPLs. The hydrodynamic particle diameters were 19 ± 1 nm at 0.27% Polydispersity index (PDI) (AuNPs in water) and 30 ± 2 nm at 0.44% PDI (TPLs in saline), as shown in Fig. 1D. This result indicates that TPLs are stable in saline. Additionally, phosphatidylglycerols (PG) (10:0, 12:0, 14:0, 16:0, and 18:0), phosphatidic acids (PA) (6:0, 8:0, 10:0, 12:0, 14:0, and 16:0), and phosphatidylserine (PS) (8:0, 10:0, 12:0, 14:0, and 16:0) were investigated. Consequently, PA(10:0)-, PS(14:0)-, and PG(16:0)-coated AuNPs are observed (Supplementary Fig. 1A). AuNP/PC(10:0)/Apo-A1 and AuNP/PC(10:0)/Apo-E4 were also produced and characterized (Supplementary Fig. 1B). Thus, we developed a specific nanotechnique for TPL-preparation that is based on a self-assembly process.

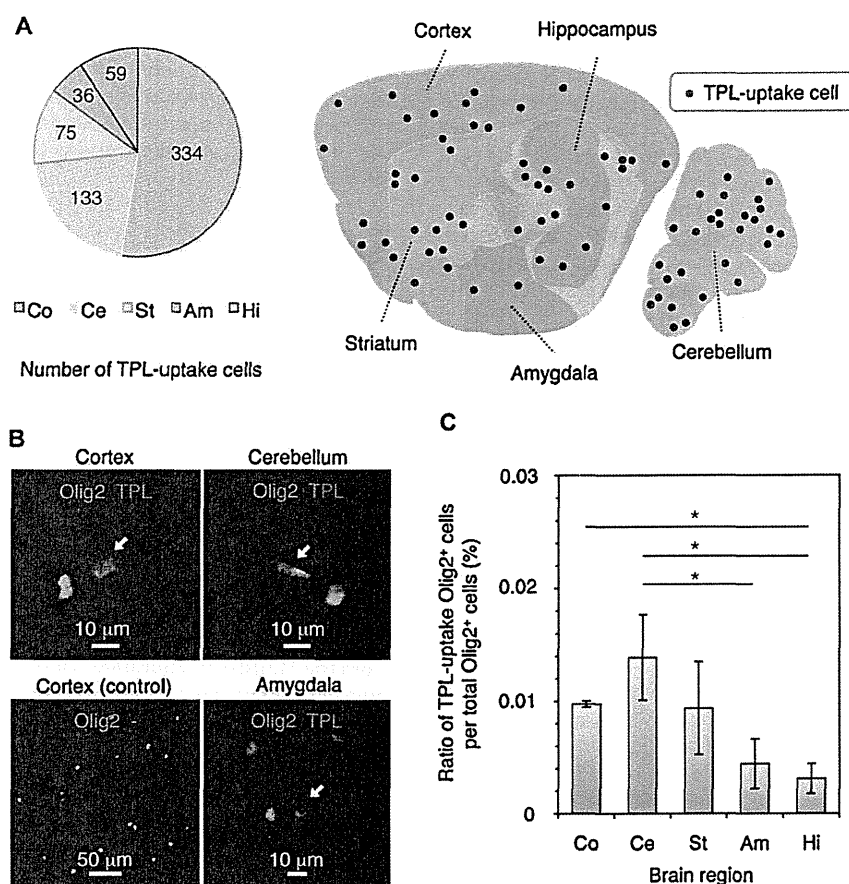Supplementary data associated with this article can be found, in the online version, at http://dx.doi.org/10.1016/j.colsurfa.2013.05.053.

Fig. 3. Analyses of tunable plasma lipoproteins in the brain. (A) Pie graph showing the number of cells in the brain with TPL-uptake (cortex: Co, cerebellum: Ce, striatum: St, amygdala: Am, and hippocampus: Hi). Schematic of the mouse brain showing localized TPL; width of 360 μm. (B) Fluorescent microscopy images of TPL-uptake cells that expressed oligodendrocyte transcription factor2 (Olig2). Green (λ_{Ex} = 495 nm, λ_{Em} = 519 nm for Alexa Fluor® 488) represents Olig2. Red signals indicate TPLs labeled with the cell tracker, CM-DiI (λ_{Ex} = 553 nm, λ_{Em} = 570 nm). Arrows show the TPL-uptake Olig2$^+$ cells. In order to analyze the fluorescent signals of TPL uptake cells while reducing intrinsic fluorescent signals we make a 10 μm section. At this thickness it is usually only possible to find one TPL uptake cell within a section. With a thicker section we would be less likely to be able to detect TPLs. Thus, it is only possible to produce an image of a single cell. (C) Ratio of TPL uptake into Olig2$^+$ cells per total Olig2$^+$ cells in different regions of the brain (cortex: Co, cerebellum: Ce, striatum: St, amygdala: Am, and hippocampus: Hi). Asterisk indicates there were larger numbers of TPL-uptake Olig2$^+$ cells in the cerebellum than the amygdala and hippocampus, and in the cortex than the hippocampus. Each data point represents the mean ± S.D. of n = 3 mice (100 serial sagittal sections per mouse). *$P < 0.05$ by Tukey's test.

3.2. Internalization of tunable plasma lipoproteins in endothelial cells

The transcytotic pathway of TPL: AuNP/PC(10:0)/Apo-B100 into endothelial cells (ECs) was elucidated in vitro with caveolin-coated vesicles (CAVs) and clathrin-coated vesicles (CLVs), which are capable of mediating transcytosis from blood to the brain [21]. Immunocytochemical analyses (Fig. 2A) revealed the internalization of TPLs at the incubation times of 6 h (caveolin images) and 12 h (clathrin images). Additionally, confocal microscopy images of control (without TPLs) and negative control (without antibodies or without TPLs and antibodies) are shown. A TEM image of TPL-including example of intracellular vesicle was observed. To analyze the uptake and efflux of TPLs in the ECs, total intensity of the DiI-signals from TPLs that internalized into the ECs were quantified. ECs that grew to sub-confluence were treated with TPLs with a final mass concentration of 2.5 μg/ml cell culture medium for 12 h. The TPL-containing cell culture medium was replaced with non-TPL-enriched cell medium after 12 h of incubation. As shown in Fig. 2C, we found a reduction in the quantity of TPLs to 70% after 30 min. This result indicates that CAVs and CLVs in ECs play a role as frequent uptake and efflux carriers for TPLs. Low-density lipoprotein receptor-related protein 8 (LRP8) and low-density lipoprotein receptor (LDLR) were investigated

to identify a receptor that could be associated with TPLs in the ECs. It is generally known that LRP8 and LDLR are required for endocytosis of LDLs [22,23]. Moreover, LRP8 is localized in CAVs, gene expression of LRP8 in mouse brain ECs is higher than LRP1, LRP2, and LDLR, and LRP8 in mouse brain ECs is enriched in comparison to LRP8 in liver or lung ECs [23,24]. Consequently, we chose the LRP8 and LDLR in established brain endothelial cell line (bEnd.3 cells). From the observations of LRP8 and LDLR in ECs, TPLs were recognized by LRP8 but not LDLR (Fig. 2E). Hence, TPLs could acquire an EC recognition ability in the same way as PLs by the tuning of PL components on the AuNP surfaces. Additionally, AuNP/PC(10:0)/Apo-A1 and AuNP/PC(10:0)/Apo-E4 were also elucidated in vitro. Consequently we found that they internalized into ECs via the CAVs and CLVs (Supplementary Fig. 2A). A reduced quantity of AuNP/PC(10:0)/Apo-A1 to 63% and AuNP/PC(10:0)/Apo-E4 to 78% were also shown (Supplementary Fig. 2B). These results indicate that both Apo-A1 and Apo-E4 have similar characteristics to Apo-B100 for the internalization of TPLs into ECs.

3.3. The brain cell specificity of tunable plasma lipoproteins

To confirm transportation of TPL: AuNP/PC(10:0)/Apo-B100 across the BBB, counts of cells which had successfully taken-up TPLs (TPL-uptake cells) were obtained in serial sagittal brain sections at

a thickness of 10 μm. Using a Plan Apo 20× objective lens, the optical fields were scanned in all areas of the brain sections. The DiI induced fluorescent signals of TPLs in the sections were compared to saline injected sections and distinguished from the intrinsic fluorescent signals (Supplementary Fig. 3A). As shown in Fig. 3A, we found TPL-uptake cells in the cortex (334 cells), the cerebellum (133 cells), striatum (75 cells), amygdala (36 cells), and hippocampus (59 cells) from the observation of whole brain sections (895 pieces) treated with a 12.5 μg TPL injection. Additionally TPL-accumulated regions with a width of 360 μm are shown. To identify the types of neural cells, we examined the oligodendrocyte transcription factor 2 (Olig2) in TPL-uptake cells using an immunohistochemical analysis. Olig2, which is the basic helix-loop-helix transcription factor, is essential for specification and maturation of astrocytes and oligodendrocytes [25–27]. Olig2$^+$ cells are defined as immature oligodendrocyte precursor cells (OPCs) (also known as NG2 cells) [25–27]. From the analyses of 100 serial sagittal sections, we found TPL-uptake cells (102 cells), 54% of which were identified as Olig2$^+$ cells, and 42% of which were identified as brain-ECs (Fig. 3B and Supplementary Fig. 3B). The brain ECs were shown using staining by FITC-conjugated TOMATO lectin (a known endothelial cell marker). Fluorescent images of Olig2$^+$ cells (without TPLs) in the cortex are shown (control). Moreover, Fig. 3C shows there were larger numbers of TPL-uptake Olig2$^+$ cells in the cerebellum than the amygdala and hippocampus, and in the cortex than the hippocampus at the 25 μg TPL injection amount (100 serial sagittal sections per mouse, n = 3 mice). Although we found low numbers of TPL-uptake Olig2$^+$ cells (Fig. 3C), this finding would be explained by the comparison of TPLs with LDLs. In fact, the TPL-injected mass (M) of 25 μg was used. However, the naturally occurring LDL mass (M) was 135 μg in 5 week-old mouse plasma (exact LDL mass was adapted from [28]). Hence, total particle numbers (N) of TPLs and LDLs can be calculated as follows:

$$N = \frac{M}{\rho V}$$

where V is the volume per a TPL (particle diameter: 30 nm) and an LDL (particle diameter: 21–27 nm), ρ is the density of a TPL (19.32 g/cm^3: gold) or an LDL (1.019–1.063 g/cm^3). Calculated data show that total particle numbers of TPLs (particle number: 9.2×10^{10} counts) were 200 times lower compared with those of LDLs (particle number: 1.9×10^{13} counts). Therefore, this analysis enabled us to calculate the mean for low numbers of TPL-uptake Olig2$^+$ cells. Therefore, our study is the first evidence that tuning of PCs and Apo-B100 on nanoparticle surfaces is especially helpful for delivery route of glial cell.

Supplementary data associated with this article can be found, in the online version, at http://dx.doi.org/10.1016/j.colsurfa.2013.05.053.

4. Conclusions

Malfunction of glial cells is a serious risk factor for NDs like AD, PD, and SCA generation and should be targeted for therapeutic intervention. At present, it is difficult to adequately treat these diseases with clinical therapies and medication. Nanoparticles will enhance and enable novel possibilities in the research area of medicine. We constructed specific TPLs and clearly demonstrated their pathways to the brain and delivery to glia cells. Our results show that TPL-accumulations occur especially in AD, PD, and SCA generation regions in the brain. Hence, these findings offer the potential to specifically control regions of ND generation. Furthermore, glial cells, which had taken-up TPLs, may relate to brain self-organizing processes (BSOPs), which are produced and preserved by cerebral sustenance transportation across the BBB. TPLs may help to fight AD, PD, and SCA by elucidation of the link between

TPLs and BSOPs, since AuNPs, which are used to assemble the TPL cores, are attractive as a contrast agent for X-ray CT-imaging. We expect that investigations into the adjustment or tuning of TPLs will lead to key advances for human applications in the development of effective ND theranostic methods, improve monitoring and analysis of glial cells, and allow access to innovative neurobiological information.

References

[1] H. van Praag, G. Kempermann, F.H. Gage, Neural consequences of environmental enrichment, Nat. Rev. Neurosci. 1 (2000) 191–198.
[2] N.J. Abbott, L. Rönnbäck, E. Hansson, Astrocyte-endothelial interactions at the blood–brain barrier, Nat. Rev. Neurosci. 7 (2006) 41–53.
[3] B.A. Barres, The mystery and magic of glia: a perspective on their roles in health and disease, Neuron 60 (2008) 430–440.
[4] R.J.M. Franklin, C. Ffrench-Constant, Remyelination in the CNS: from biology to therapy, Nat. Rev. Neurosci. 9 (2008) 839–855.
[5] M. Maden, Retinoic acid in the development regeneration and maintenance of the nervous system, Nat. Rev. Neurosci. 8 (2007) 755–765.
[6] F. Taroni, S. DiDonato, Pathways to motor incoordination: the inherited ataxias, Nat. Rev. Neurosci. 5 (2004) 641–655.
[7] H.J. Kayden, M.G. Traber, Absorption lipoprotein transport, and regulation of plasma concentrations of vitamin E in humans, J. Lipid Res. 34 (1993) 343–358.
[8] R.W. Mahley, T.L. Innerarity, Lipoprotein receptors and cholesterol homeostasis, Biochim. Biophys. Acta 737 (1983) 197–222.
[9] B.A. Barres, M.A. Lazar, M.C. Raff, A novel role for thyroid hormone glucocorticoids and retinoic acid in timing oligodendrocyte development, Development 120 (1994) 1097–1108.
[10] J.D. Cahoy, B. Emery, A. Kaushal, L.C. Foo, J.L. Zamanian, K.S. Christopherson, Y. Xing, J.L. Lubischer, P.A. Krieg, S.A. Krupenko, W.J. Thompson, B.A. Barres, A transcriptome database for astrocytes neurons, and oligodendrocytes: a new resource for understanding brain development and function, J. Neurosci. 28 (2008) 264–278.
[11] K. Lipponen, P.W. Stege, G. Cilpa, J. Samuelsson, T. Fornstedt, M.-L. Riekkola, Three different approaches for the clarification of the interactions between lipoproteins and chondroitin-6-sulfate, Anal. Chem. 83 (2011) 6040–6046.
[12] J. Kreuter, Nanoparticulate systems for brain delivery of drugs, Adv. Drug. Delivery. Rev. 47 (2001) 65–81.
[13] J. Kreuter, D. Shamenkov, V. Petrov, P. Ramge, K. Cychutek, C. Koch-brandt, R. Alyautdin, Apolipoprotein-mediated transport of nanoparticle-bound drugs across the blood–brain barrier, J. Drug Target. 10 (2002) 317–325.
[14] D. Begley, Delivery of therapeutic agents to the central nervous system: the problem and the possibilities, Pharm. Ther. 104 (2004) 29–45.
[15] A. Zensi, D. Begley, C. Pontikis, C. Legros, L. Mihoreanu, S. Wagner, C. Büchel, H. von Briesen, J. Kreuter, Albumin nanoparticles targeted with Apo E enter the CNS by transcytosis and are delivered to neurons, J. Control. Release 137 (2009) 78–86.
[16] D.P. Cormode, T. Skajaa, M.M. van Schooneveld, R. Koole, P. Jarzyna, M.E. Lobatto, C. Calcagno, A. Barazza, R.E. Gordon, P. Zanzonico, E.A. Fisher, Z.A. Fayad, W.J.M. Mulder, Nanocrystal core high-density lipoproteins: a multimodality contrast agent platform, Nano Lett. 8 (2008) 3715–3723.
[17] D.P. Cormode, E. Roessl, A. Thran, T. Skajaa, R.E. Gordon, J. Schlomka, V. Fuster, E.A. Fisher, W.J.M. Mulder, R. Proksa, Z.A. Fayad, Atherosclerotic plaque

composition: analysis with multicolor CT and targeted gold nanoparticles, Radiology 256 (2010) 774–782.

[18] B.Y.S. Kim, J.T. Rutka, W.C.W. Chan, Nanomedicine, N. Engl. J. Med. 363 (2010) 2434–2443.

[19] G. Frens, Controlled nucleation for the regulation of the particle size in monodisperse gold suspensions, Nature 241 (1973) 20–22.

[20] S.L. Goodman, G.M. Hodges, D.C. Livingston, A review of the colloidal gold marker system, Scan. Electron Microsc. 11 (1980) 133–146.

[21] F. Hervé, N. Ghinea, J. Scherrmann, CNS delivery via adsorptive transcytosis, AAPS. J. 10 (2008) 455–472.

[22] W.J. Schneider, J. Nimpf, LDL receptor relatives at the crossroad of endocytosis and signaling, Cell. Mol. Life Sci. 60 (2003) 892–903.

[23] D.R. Riddell, X.M. Sun, A.K. Stannard, A.K. Soutar, J.S. Owen, Localization of apolipoprotein E receptor 2 to caveolae in the plasma membrane, J. Lipid Res. 42 (2001) 998–1002.

[24] R. Daneman, L. Zhou, D. Agalliu, J.D. Cahoy, A. Kaushal, B.A. Barres, The mouse blood–brain barrier transcriptome: a new resource for understanding the development and function of brain endothelial cells, PLoS One 5 (2010) e13741.

[25] C.A. Marshall, B.G. Novitch, J.E. Goldman, Olig2 directs astrocyte and oligodendrocyte formation in postnatal subventricular zone cells, J. Neurosci. 25 (2005) 7289–7298.

[26] J. Cai, Y. Chen, W.H. Cai, E.C. Hurlock, H. Wu, S.G. Kernie, L.F. Parada, Q.R. Lu, A crucial role for olig2 in white matter astrocyte development, Development 134 (2007) 1887–1899.

[27] X. Zhu, H. Zuo, B.J. Maher, D.R. Serwanski, J.J. LoTurco, Q.R. Lu, A. Nishiyama, Olig2-dependent developmental fate switch of NG2 cells, Development 139 (2012) 2299–2309.

[28] S. Qiu, N. Bergeron, L. Kotite, R.M. Krauss, A. Bensadoun, R.J. Havel, Metabolism of lipoproteins containing apolipoprotein B in hepatic lipase-deficient mice, J. Lipid Res. 39 (1998) 1661–1668.

PARTICLE AND
FIBRE TOXICOLOGY

RESEARCH   Open Access

Effect of aerosol particles generated by ultrasonic humidifiers on the lung in mouse

Masakazu Umezawa[1,2*†], Keisuke Sekita[1†], Ken-ichiro Suzuki[2], Miyoko Kubo-Irie[2], Rikio Niki[2], Tomomi Ihara[3], Masao Sugamata[3] and Ken Takeda[1,2]

Abstract

Background: Ultrasonic humidifiers silently generate water droplets as a cool fog and produce most of the dissolved minerals in the fog in the form of an aerosolized "white dust." However, the health effect of these airborne particles is largely unknown. This study aimed to characterize the aerosol particles generated by ultrasonic humidifiers and to investigate their effect on the lung tissue of mice.

Methods: An ultrasonic humidifier was operated with tap water, high-silica water, ultrapure water, or other water types. In a chamber (0.765 m^3, ventilation ratio 11.5 m^3/hr), male ICR mice (10-week-old) were exposed by inhalation to an aerosol-containing vapor generated by the humidifier. After exposure for 7 or 14 days, lung tissues and bronchoalveolar lavage fluid (BALF) were collected from each mouse and examined by microarray, quantitative reverse transcription-polymerase chain reaction, and light and electron microscopy.

Results: Particles generated from the humidifier operated with tap water had a mass concentration of 0.46 ± 0.03 mg/m^3, number concentration of $(5.0 \pm 1.1) \times 10^4$/$cm^3$, and peak size distribution of 183 nm. The particles were phagocytosed by alveolar macrophages in the lung of mice. Inhalation of particles caused dysregulation of genes related to mitosis, cell adhesion molecules, MHC molecules and endocytosis, but did not induce any signs of inflammation or tissue injury in the lung.

Conclusion: These results indicate that aerosol particles released from ultrasonic humidifiers operated with tap water initiated a cellular response but did not cause severe acute inflammation in pulmonary tissue. Additionally, high mineral content tap water is not recommended and de-mineralized water should be recommended in order to exclude any adverse effects.

Background

The indoor air environment is important for human health because humans spend most of their time indoors [1]. Volatile organic compounds [2], microorganisms [3], environmental allergens [4], and particle matter [5] have been reported as important factors of the indoor environment. It is necessary to conduct safety assessments of consumer products, e.g., air conditioners, humidifiers, and air purifiers, which are all prevalent in commercial facilities, hospitals, schools, and homes.

The most important factors of the indoor air environment are temperature and humidity [6,7]. Humidifiers are used to prevent excessive drying and to maintain comfortable room humidity. There are three types of humidifier: evaporative, steam, and ultrasonic vaporizers [8]. While ultrasonic humidifiers need little electricity to work and release cooler vapor than the steam-type, they must be cleaned to avoid bacterial contamination since the vapor contains all impurities that are present in the reservoir [9,10]. Only ultrasonic humidifiers release most of the dissolved and suspended components of the water, including microorganisms and pathogens, into the air [11]. Fatal pulmonary damage, i.e., rapidly progressive respiratory fibrosis, has also been reported when a water aerosol which contained biocides was released from humidifiers and was inhaled by humans [12].

* Correspondence: masa-ume@rs.noda.tus.ac.jp
†Equal contributors
[1]Department of Hygienic Chemistry, Faculty of Pharmaceutical Sciences, Tokyo University of Science, 2641 Yamazaki, Noda, Chiba 278-8510, Japan
[2]The Center for Environmental Health Science for the Next Generation, Research Institute for Science and Technology, Tokyo University of Science, 2641 Yamazaki, Noda, Chiba 278-8510, Japan
Full list of author information is available at the end of the article

Even if the water has no contamination by microorganisms or pathogens, ultrasonic humidifiers may exert some effects on human health. Previous studies showed that ultrasonic humidifiers may release dissolved minerals as an aerosol [13]. Highsmith et al. [14] reported that the fine particle concentration exceeded 6.3 mg/m^3 when an ultrasonic humidifier was operated in a closed room. A subsequent study reported that the "white dust" induced lung injury [15]. However, the detailed components of the aerosol (or dust) and its health effect (e.g., inflammatory response in the lung) remained unknown. The aim of the present study was to characterize the aerosol particles generated by an ultrasonic humidifier and to investigate their effects on the lung in a mouse model.

Methods

Ultrasonic humidifier operation

An ultrasonic humidifier, BBH-07 (Hanwa Ltd., Osaka, Japan) was placed in each chamber with a volume of 0.765 m^3 and a ventilation ratio of 11.5 m^3/hr in the Center for Environmental Health Science for the Next Generation (Research Institute for Science and Technology, Tokyo University of Science, Noda, Chiba, Japan). The humidifier was operated at approximately 60 mL/hr liquid output rate with one of the following types of water: tap water obtained in Noda-city (Chiba, Japan), high-silica water purchased from Riken Mineral Kenkyusho K.K (Ebino, Miyazaki, Japan), a graded series of calcium chloride solution (4–400 mg/L of calcium), reverse osmotic membrane-filtration water (RO water) purchased from Ako Kasei Co., Ltd. (Ako, Hyogo, Japan), or an ultrapure water generated by an Automatic Sanitization Module (Merck Millipore, Billerica, MA, USA). Tap water and high-silica water were examples of drinking water containing minerals, while the calcium chloride solutions were used as a model of mineral-dissolved water with known concentrations. The concentration of Na, Ca, Mg, and Si in each type of water was measured using inductively coupled plasma mass spectrometry (ICP-MS) by Murata Keisokuki Service Co., Ltd. (Kanagawa, Japan). The humidifier was operated at approximately 80% power.

Characterization of particles from the humidifier

The mass concentration of particles in the chamber was measured by a Piezobalance dust monitor Model 3521 (Kanomax Japan Inc., Osaka, Japan). The number concentration of particles was measured by a portable particle counter CPC 3007 (Tokyo Dylec Co., Tokyo, Japan), which can count particles with 10–1000 nm diameter. The size distribution of particles (10–410 nm) was measured by a switch-mode power supplies system Model 3936 (TSI Inc., Shoreview, MN, USA) composed of a classifier DMA3081 (TSI Inc.) and a condensation particle counter CPC 3785 (TSI Inc.) at a flow rate of 0.6 L/min.

Airborne particles in the chamber were classified using a cascade impactor (NL-3-2.5c0.5c, Tokyo Dylec). Fractions of 0.5 – 2.5 μm and <0.5 μm were collected for 30 sec and 15 min, respectively, at a flow rate of 0.3 L/min. The fractionated particles were collected on a silicon wafer (SI-500452, Nilaco Co., Tokyo, Japan) or a collodion film-patched mesh (200 mesh Cu; Nisshin EM Co., Tokyo, Japan) by electrostatic force using a sampler for suspended particle matter, SSPM-100 (Shimadzu Co., Kyoto, Japan). To determine the form and elemental component of the particles, they were observed by a field emission-type scanning electron microscope/energy-dispersive X-ray spectrometer (FE-SEM/EDS) (JSM-6500 F, JEOL Ltd., Akishima, Tokyo, Japan) with accelerating voltage of 15.0 kV and a transmission electron microscope (TEM: JEM-1200EX II, JEOL) with accelerating voltage of 90.0 kV.

Exposure of mice to particles released from an ultrasonic humidifier

All animals were treated and handled in accordance with the national guidelines for care and use of laboratory animals and with the approval of the Tokyo University of Science Institutional Animal Care and Use Committee. Male ICR mice (10 weeks old) were purchased from Japan SLC Inc. (Hamamatsu, Shizuoka, Japan) and housed in a controlled room with *ad libitum* access to chow and water. After acclimation for 7 days, they were exposed by inhalation to an aerosol-containing vapor generated by an ultrasonic humidifier. The relative humidity was approximately 75% in the chamber with operating the humidifier. Tap water obtained in Noda-city, high-silica water, or ultrapure water were used to operate the ultrasonic humidifier for 7 days (8 hr/day [10:00 am – 6:00 pm] or whole day) or 14 days (whole day) (Table 1). After each exposure period, lung tissues and bronchoalveolar lavage fluid (BALF) were collected from each mouse under anesthesia by intraperitoneal injection of pentobarbital sodium.

BALF cell analysis

The cells in BALF were collected by centrifugation at $1,000 \times g$ for 10 min and resuspended in phosphate-

Table 1 Experimental conditions for analysis of the effect of particles generated by ultrasonic humidifier on mouse lung

	Exposure time	Tested water
Experiment 1	8 hr/day, 7 days	Tap water/Ultrapure water
Experiment 2	8 hr/day, 7 days	High-silica water/Ultrapure water
Experiment 3	24 hr/day, 7 days	Tap water/Ultrapure water
Experiment 4	24 hr/day, 7 days	High-silica water/Ultrapure water
Experiment 5	24 hr/day, 14 days	High-silica water/Ultrapure water

buffered saline (pH 7.4). After counting the total number of cells, they were observed in a Giemsa-stained smear on a glass slide under a light microscope (BX51; Olympus Co., Tokyo, Japan). Statistical analysis was performed using an unpaired *t*-test and the level of significance was set at P < 0.05.

Total RNA isolation

Lung tissue was homogenized in Isogen (Nippon Gene Co., Ltd., Tokyo, Japan). Total RNA was isolated by chloroform, purified by isopropanol, precipitated in 70% ethanol according to the manufacturer's protocol and then suspended in RNase-free water. The RNA quantity was determined by absorption spectrophotometry at OD260 in a BioPhotometer plus (Eppendorf, Hamburg, Germany). Isolated RNA from each sample was provided for quantitative RT-PCR and microarray analyses.

Complementary DNA microarray

Total RNAs ($n = 4 - 5$/group) were pooled (45 μg) for each group and purified by RNeasy Micro Kit (Qiagen, Hilden, Germany). The integrity of RNA was evaluated by Bioanalyzer 2100 (Agilent Technologies Inc., Santa Clara, CA, USA). Complementary-DNA (cDNA) of each of the RNA samples was labeled by Cy3 and hybridized to the SurePrint G3 Mouse Gene Expression 8 × 60 K Microarray (Agilent Technologies) consisting of 62976 spots (containing probes for 24163 mRNAs) according to the protocol of Oncomics Co. Ltd. (Nagoya, Aichi, Japan). The microarray was then washed using Gene Expression Wash Pack (Agilent Technologies) and scanned by a DNA Microarray Scanner (Agilent Technologies). Scanner output images were normalized and digitalized by Feature Extraction software (Agilent Technologies) according to the Minimum Information About a Microarray Experiment (MIAME) guidelines [16].

Hierarchical cluster analysis

To extract gene sets for which differential expression was induced by airborne particles generated by the ultrasonic humidifier, microarray data from experiments 1–5 (Table 1) were hierarchically clustered using a complete linkage algorithm and Euclidean distance as the distance metric [17]. The analysis was performed using Cluster 3.0 [18] and the result was visualized by Java TreeView [19].

Functional analysis of microarray data

To better understand the biological meaning of the microarray results, functional analysis was performed using gene annotation by gene ontology (GO) and pathway. Genes were annotated with GO and pathway using an annotation file (gene2go.gz) provided by the National Center for Biotechnology Information (NCBI; Bethesda, MD, USA) [20] and c2.cp.v3.1.symbols.gmt by the Broad Institute

(Cambridge, MA, USA) [21]. The annotations were updated on March 6, 2013. Enrichment factors for each GO and pathway were defined as $(nf/n)/(Nf/N)$, where *nf* is the number of flagged (differentially expressed) genes within the category, *Nf* is the total number of genes within that same category, *n* is the number of flagged genes on the entire microarray, and *N* is the total number of genes on the microarray. Statistical analysis was done with Fisher's exact test based on a hypergeometric distribution and then the GO and pathways with enrichment factors ≥3, *nf* ≥3 and *P* <0.01 were extracted.

Quantitative RT-PCR

Total RNA (1 μg) for each sample was treated by Dnase (Promega Co., Fitchburg, WI, USA) and then by M-MLV reverse transcriptase (Invitrogen Co., Carlsbad, CA, USA) to obtain first strand cDNA according to the manufacturer's instructions. Quantitative PCR was performed in a 96-well plate and an Mx3000P (Agilent Technologies) with SYBR Green Realtime PCR Master Mix (Thunderbird; Toyobo Co., Ltd., Osaka, Japan) and specific primers (Fasmac Co. Ltd., Atsugi, Kanagawa, Japan) or with Probe qPCR Master Mix (Thunderbird; Toyobo Co.) and primer (Fasmac)/probe (Biosearch Technologies Japan, Inc., Tokyo, Japan) sets for indicated genes (Additional file 1: Table S1). Statistical analysis was performed using an unpaired *t*-test and the level of significance was set at P < 0.05.

Immunohistochemistry

Lung tissue was fixed in phosphate-buffered (pH7.4) 4% formaldehyde, and then cryoprotected in phosphate-buffered 30% sucrose solution for 24–48 hr. Next, brains were frozen and cut into 4-μm sections using a cryostat (Tissue-Tek Cryo; Sakura Finetek Japan). Immunohistochemical visualization of a macrophage marker, F4/80, was performed using antibodies and avidin – biotin-peroxidase methods. After blocking endogenous peroxidase and preincubation with 10% normal horse serum, sections were treated overnight with primary rat monoclonal anti-F4/80 antibody (ab6640; Abcam plc, Cambridge, UK), secondary biotinylated donkey anti-rat IgG (AP189B; Merck Millipore) for 2 hr, and finally treated with an avidin – biotin-peroxidase complex (Vectastain ABC peroxidase kit, Vector Laboratories, CA, USA) for 4 hr. Sections were then reacted for peroxidase activity in a solution of 0.04% 3,3′-diaminobenzidene (DAB) in 0.1 M Tris–HCl buffer (pH 7.6) and 0.01% hydrogen peroxide water. Immunoreactive cells on sections were observed under BX51 light microscope. Quantitative analysis was performed on all sections. Statistical analysis was performed using an unpaired *t*-test and the level of significance was set at P < 0.05.

Electron microscopic analysis

Lung tissues and BALF cells were prefixed in cacodylate-buffered 2.5% glutaraldehyde (pH 7.4) for 24 hr, washed in cacodylate buffer, and postfixed with 2% osmium tetroxide (Nisshin EM) for 1 hr. After washing in cacodylate buffer, the tissue samples were dehydrated using a graded series of ethanol (up to 100%) and propylene oxide (Nisshin EM), and then embedded in Quetol 812 (Nisshin EM). Ultra-thin sections (80-nm thick) were cut on the ultra-microtome EMUC6 (Leica Microsystems K.K., Tokyo, Japan). Some sections were double-stained with uranyl acetate and lead citrate. They were then observed under the TEM (JEM-1200EX II) with accelerating voltage of 80–90 kV.

Results

Mineral and silica concentration of each water type

Tap water, high-silica water, RO water, and ultrapure water were subjected to ICP-MS analysis to measure the concentrations of Na, Ca, Mg, and Si (SiO_2: hydrated silica) (Table 2). Tap water contained 15–25 mg/L Na, 15–30 Ca, 4–7 Mg and 20–50 SiO_2. High-silica water contained 73 mg/L SiO_2. Most of the minerals and silica were absent in RO water, which contained only (3 mg/L) Na. No minerals and silica were detected in ultrapure water.

Concentration and size distribution of particles released from humidifier

First, we determined the mass and number concentrations and the peak size distribution of particles generated by an ultrasonic humidifier that was operated with each type of water in our chamber (Table 3). The results with tap water (Noda-city, and other area for which data not shown) were: mass concentration 0.35 – 0.50 mg/m^3, number concentration 3.5 – 7.5 × 10^4 particles/cm^3, and 155–195 nm peak size distribution (number distribution). The results obtained with high-silica water were similar to tap water. The mass concentration of particles generated by the humidifier with RO water was below the detection limit (<0.01 mg/m^3) but the number concentration was similar to tap water. The size distribution pattern with tap water and high-silica water was similar to a previous report [22] (Figure 1A). The humidifier generated visible fog (micro-sized water droplets) and submicro-sized residuals; however, because the SMA-CPC system could

detect particles with diameter 10–410 nm, we characterized only the residuals as particles but not obtain size distribution data of the primary water droplets of the humidifier. The size of the particles generated by the humidifier using RO water was smaller to that of water types which contain a higher concentration of minerals and silica, e.g., tap water and high-silica water. The fog from the humidifier with ultrapure water did not contain non-volatile particles nor did it elicit any peak size distribution. The result with another type of pure water which originated from a PURELAB Option-7/15 Water Purification System (ELGA LabWater, Bucks, UK) was very similar to that with the ultrapure water (data not shown).

To investigate the correlations between mineral concentration in water and each parameter of generated particle, we characterized the particles released from the ultrasonic humidifier using water containing serial concentrations of calcium chloride solution (4–400 mg/L Ca) (Table 3). The concentration of calcium chloride in water was positively correlated with the mass and number concentrations (Figure 1C and D) and the peak size distribution (Figure 1B and E) of generated particles. The correlation of the concentration of dissolved material in water with the mass concentration of particles generated was linear (r =0.97) (Figure 1C), whereas the correlation with the number concentration was logarithmic (r =0.98) (Figure 1D). These correlations were also observed in particles from the humidifier with serial concentrations of sodium chloride solution (4–400 mg/L Na) (data not shown). The mass concentration of the aerosol particles was also correlated with total mineral concentration of tap water, high-silica water and RO water (Figure 1A).

Form and elemental composition of particles released from humidifier

FE-SEM images showed that the humidifier operated with tap water or high-silica water released a large number of spherical-formed amorphous <0.5 μm particles and 0.5 – 2.5 μm agglomerates (Figure 2A – C). The particles were deformed under extremely high humidification (Figure 2D, E). TEM images also showed that the form of particles from the humidifier operated with tap water (Figure 2F) or high-silica water (Figure 2G) were spherical. The electron density of the particles was inhomogeneous under TEM observation, indicating that the particles were

Table 2 Mass concentration of mineral and silica in each type of water

	Na (mg/L)	Ca (mg/L)	Mg (mg/L)	SiO_2 (mg/L)	Total (mg/L)
Tap water	18	25	5.6	24	73
High-silica water	15	12	3.7	73	104
RO water	3	<0.1	<0.1	<0.1	3
Ultrapure water	<0.1	<0.1	<0.1	<0.1	<0.1

Table 3 Concentration and size of airborne particles released from ultrasonic humidifier for each type of water

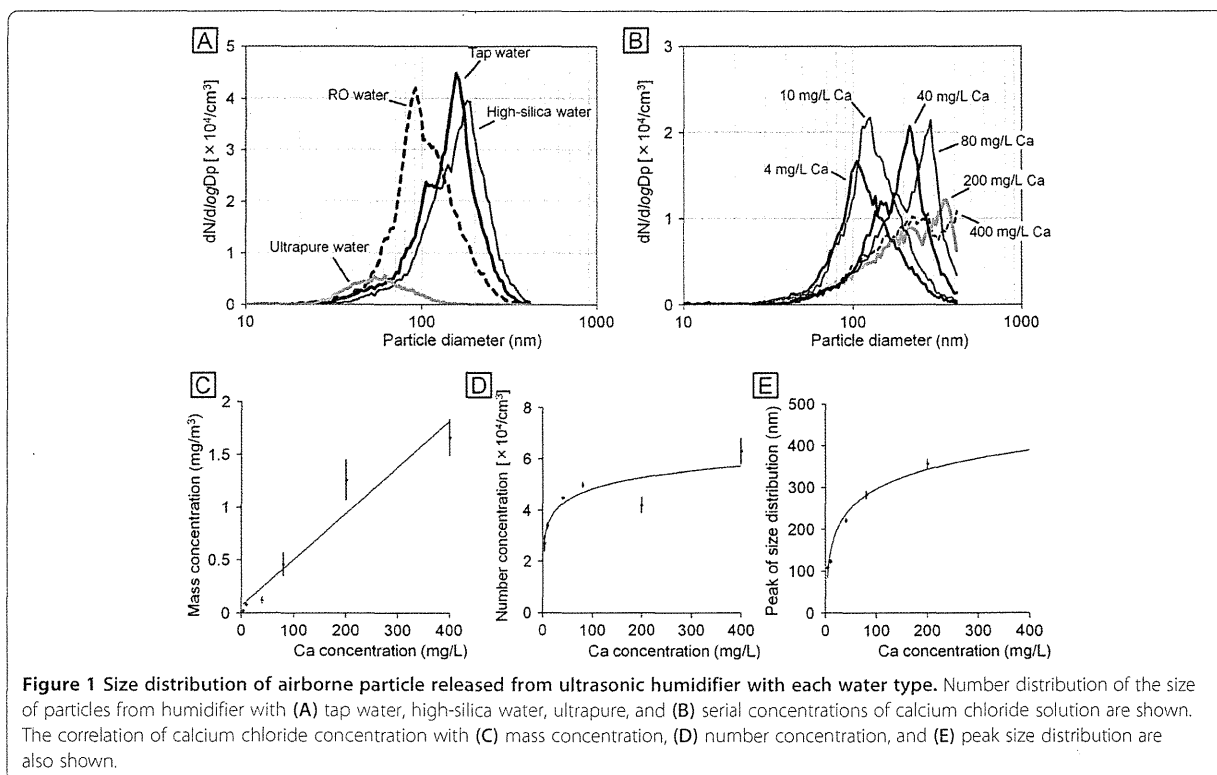| Used water	Mass concentration (mg/m^3)	Number concentration (#/cm^3)	Peak of size distribution (nm)
Tap water	0.46 ± 0.03	$(5.0 ± 1.1) × 10^4$	183 ± 9
High-silica water	0.58 ± 0.04	$(3.6 ± 0.0) × 10^4$	180 ± 3
CaCl$_2$ (400 mg/L Ca)	1.66 ± 0.16	$(6.3 ± 0.5) × 10^4$	>410
CaCl$_2$ (200 mg/L Ca)	1.26 ± 0.19	$(4.2 ± 0.3) × 10^4$	356 ± 11
CaCl$_2$ (80 mg/L Ca)	0.46 ± 0.11	$(5.0 ± 0.1) × 10^4$	283 ± 9
CaCl$_2$ (40 mg/L Ca)	0.12 ± 0.03	$(4.5 ± 0.0) × 10^4$	222 ± 4
CaCl$_2$ (10 mg/L Ca)	0.08 ± 0.01	$(3.4 ± 0.1) × 10^4$	123 ± 4
CaCl$_2$ (4 mg/L Ca)	0.02 ± 0.01	$(2.7 ± 0.3) × 10^4$	108 ± 2
RO water	<0.01	$(4.4 ± 0.6) × 10^4$	90 ± 2
Ultrapure water	<0.01	$(0.7 ± 0.0) × 10^4$	Not determined

Data are shown as mean ± SD, calculated from 5 repeats of 2 min analyses.

composed of multiple elements. EDS analysis showed the particles derived from tap water were composed of Na, Mg, Si, S (sulfate), and Ca, which were contained in tap water (Figure 2H).

Effect of particles released from ultrasonic humidifier on mRNA expression in the lung

Next, we conducted microarray analysis to investigate the effect of particles from the humidifier on the lung. The effect of the particles was determined by mRNA expression of tested water groups compared to that of ultrapure water groups in each experiment (Table 1). A total of 15984 mRNAs were detected with quantitative fluorescence signals from the lung tissue samples. Hierarchical clustering revealed that 429 mRNAs were differentially expressed (238 upregulated and 191 downregulated) by particles derived from tested water (tap water or high-silica water) (Additional file 1: Figure S1). Expression change of some genes was correlated with the dose in the experiment 2, 4 and 5 using high-silica water. These 429 genes were enriched in 17 GO (Table 4) and 12 pathways (Table 5). The largest GO and pathway were
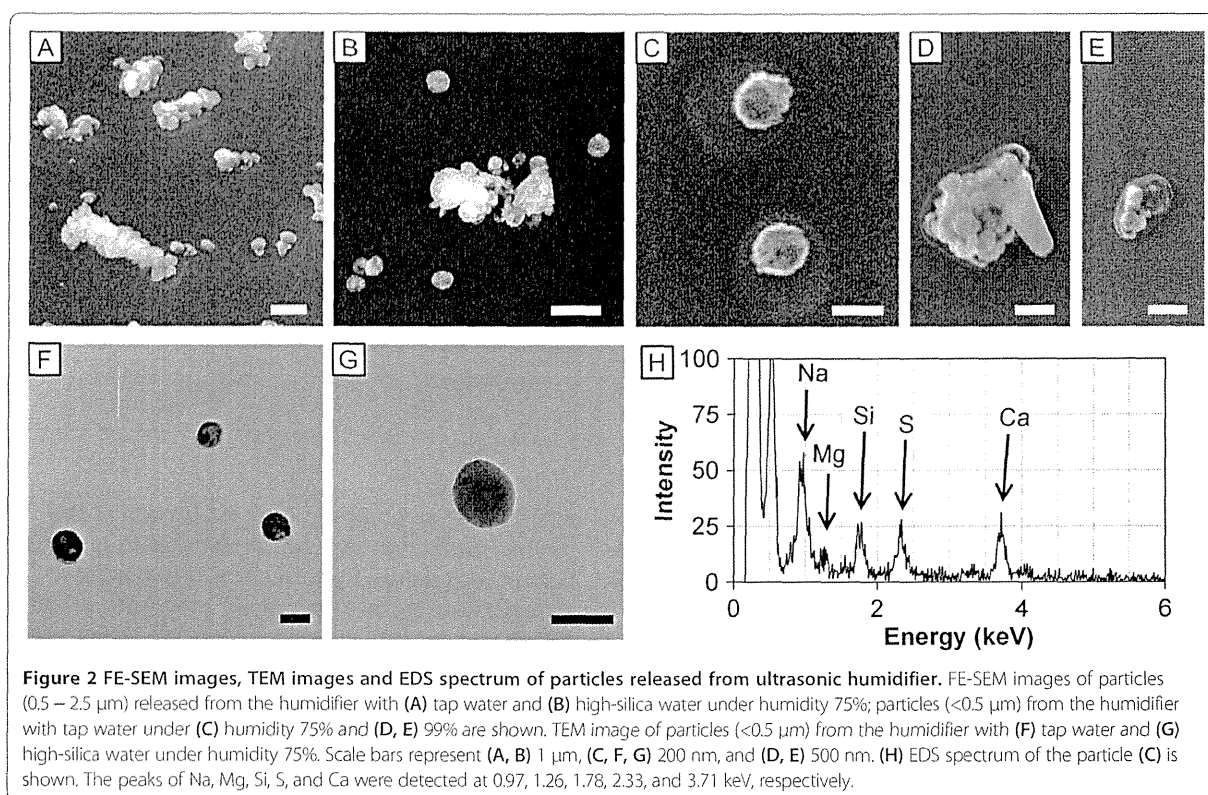

Figure 1 Size distribution of airborne particle released from ultrasonic humidifier with each water type. Number distribution of the size of particles from humidifier with **(A)** tap water, high-silica water, ultrapure, and **(B)** serial concentrations of calcium chloride solution are shown. The correlation of calcium chloride concentration with **(C)** mass concentration, **(D)** number concentration, and **(E)** peak size distribution are also shown.

Figure 2 FE-SEM images, TEM images and EDS spectrum of particles released from ultrasonic humidifier. FE-SEM images of particles (0.5 – 2.5 μm) released from the humidifier with **(A)** tap water and **(B)** high-silica water under humidity 75%; particles (<0.5 μm) from the humidifier with tap water under **(C)** humidity 75% and **(D, E)** 99% are shown. TEM image of particles (<0.5 μm) from the humidifier with **(F)** tap water and **(G)** high-silica water under humidity 75%. Scale bars represent **(A, B)** 1 μm, **(C, F, G)** 200 nm, and **(D, E)** 500 nm. **(H)** EDS spectrum of the particle **(C)** is shown. The peaks of Na, Mg, Si, S, and Ca were detected at 0.97, 1.26, 1.78, 2.33, and 3.71 keV, respectively.

Table 4 Significantly enriched GO categories from the microarray data

Gene ontology	Enrichment factor	P-value
Mitosis	3.05	<0.001
Meiosis	5.35	0.001
Regulation of axonogenesis	8.61	0.001
Antigen processing and presentation of peptide or polysaccharide antigen via MHC class II	13.7	0.001
Chromosome, centromeric region	3.50	0.001
Kinetochore	3.80	0.001
Decidualization	12.2	0.002
MHC class II protein complex	12.2	0.002
Peptide antigen binding	12.2	0.002
Platelet activation	7.32	0.002
Gamma-aminobutyric acid signaling pathway	11.0	0.002
Motile cilium	6.65	0.003
Retinol metabolic process	9.98	0.003
Adenylate cyclase-activating G-protein coupled receptor signaling pathway	6.36	0.003
Antigen processing and presentation of exogenous peptide antigen via MHC class II	8.44	0.005
Chromosome segregation	3.60	0.006
Axon part	7.32	0.007

mitosis (17 genes) and cell adhesion molecules (8 genes) (Additional file 1 Table S2). Among the 8 genes in cell adhesion molecules, upregulated *H2-DMb1* and down-regulated *H2-Ab1, H2-Eb1, H2-Q2* were associated with major histocompatibility complex (MHC) molecules, and endocytosis followed by antigen processing. Quantitative RT-PCR data showed that expression levels of a monocyte chemoattractant chemokine *Ccl2* and a chemokine related to inhalation of silica particles *Cxcl1* [23] were not affected by the particles released from the ultrasonic humidifier operated with tap water or high-silica water (Figure 3). Expression of an inflammatory cytokine *Tnf* was at quite low level in the lung of any groups.

Effect of particles released from ultrasonic humidifier on histology of the lung and alveolar macrophage

HE-stained images did not show any remarkable changes or cell proliferation in lung after inhalation of particles from the humidifier with tap water or high-silica water (24 hr/day, 7–14 days). The lung tissues obtained from experiment 5 (24 hr/day for 14 days inhalation with the commercial high-silica water *vs.* ultrapure water; Table 1) were also subjected to analysis by immunohistochemistry and TEM. TEM observation of the lung tissues (Figure 4A) and BALF cells (Figure 4B) revealed that alveolar macrophages endocytosed the particles. The endocytosed particles showed a high contrast without staining by uranyl

Table 5 Significantly enriched pathways from the microarray data

Pathway	Enrichment factor	P-value
CENP-A NAC-CAD complex (MIPS)	16.2	<0.001
PLK1 pathway (PID)	6.85	<0.001
Asthma (KEGG)	12.1	0.002
Cell adhesion molecules (KEGG)	3.53	0.002
Viral myocarditis (KEGG)	4.31	0.003
Allograft rejection (KEGG)	5.94	0.004
Mitotic prometaphase (Reactome)	3.66	0.006
Autoimmune thyroid disease (KEGG)	5.40	0.006
Graft versus host disease (KEGG)	5.40	0.006
GA13_PATHWAY (STKE)	5.24	0.007
Antigen processing and presentation (KEGG)	3.98	0.008
Type I Diabetes Mellitus (KEGG)	4.95	0.008

Contributors for curation: KEGG, KEGG: Kyoto Encyclopedia of Genes and Genomes; MIPS, MIPS database from CORUM (the Comprehensive Resource of Mammalian protein complexes); PID, Pathway Interaction Database (National Cancer Institute and Nature Publishing Group); STKE, Signal Transduction Knowledge Environment.

acetate and lead citrate (Figure 4A, insert), indicating that the particles were mineral particles rather than endogenous biomolecules. The diameter of the particles deposited in the lung was mostly within the range of 100–200 nm (Figure 4B, insert), and dissolving particles with approximately 20–60 nm diameter were also found in intracellular vesicles in the macrophage (Figure 4A, insert). The number of F4/80 positive cells (macrophages) did not significantly differ between ultrapure water and high-silica water groups by 14-day inhalation of the particles (Figure 4C – E). Abnormal macrophage accumulation was not observed in the lung of treated group. Although the total number of BALF cells was not affected by inhalation of particles from the humidifier with high-silica water (data not shown), the ratio of mononuclear

cells in BALF tended to be increased ($P =0.08$) by 14-day inhalation of the particles (Figure 4F).

Discussion

Tap water contains dissolved solid composed of calcium, sodium, other minerals and anions. The secondary water quality standard of total dissolved solids (TDS) is established as 500 mg/L by the Ministry of Health, Labour and Welfare (Japan) and the Environmental Protection Agency (US). Water also has 'hardness', which is definable as the concentration of resistant solid matter determined as the equivalent concentration of calcium carbonate. Since the concentration and size distribution of particles from ultrasonic humidifier were well correlated with the concentration of minerals, they can be estimated by the TDS and hardness of water provided to the humidifier.

Humidifiers are usually operated with tap water, and in these experiments we found that operation with tap water generated submicron-sized particles (100–1000 μm), which contribute to the mass concentration, and that the humidifier released them into the air. In contrast, the particles from the humidifier operated with water containing a low concentration of minerals (4 mg/L Na or Ca) were mostly nano-sized (<100 nm); therefore they had only a small mass (<0.03 mg/m^3) but a large number concentration (>2 × 10^4/cm^3). This is the first study showing the characteristics of particles from the humidifier with tap water as well as other water with a low concentration of minerals. In the study using a series of calcium chloride solutions, the mass and the number concentrations were not well correlated. We concluded the cause of this worse correlation was another correlation between the mineral concentration of water and the particle size; i.e., the size was larger when the humidifier was operated with a water with higher concentration of minerals. Our data for the concentration of particles from ultrasonic humidifiers were measured in an experimental chamber (0.765 m^3, ventilation ratio 11.5 m^3/hr), whereas 0.59 mg/m^3, which
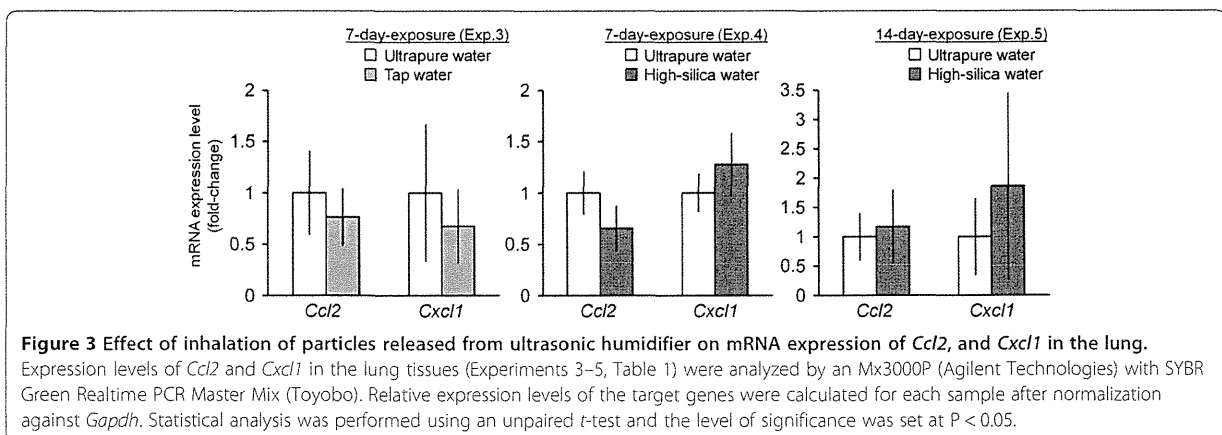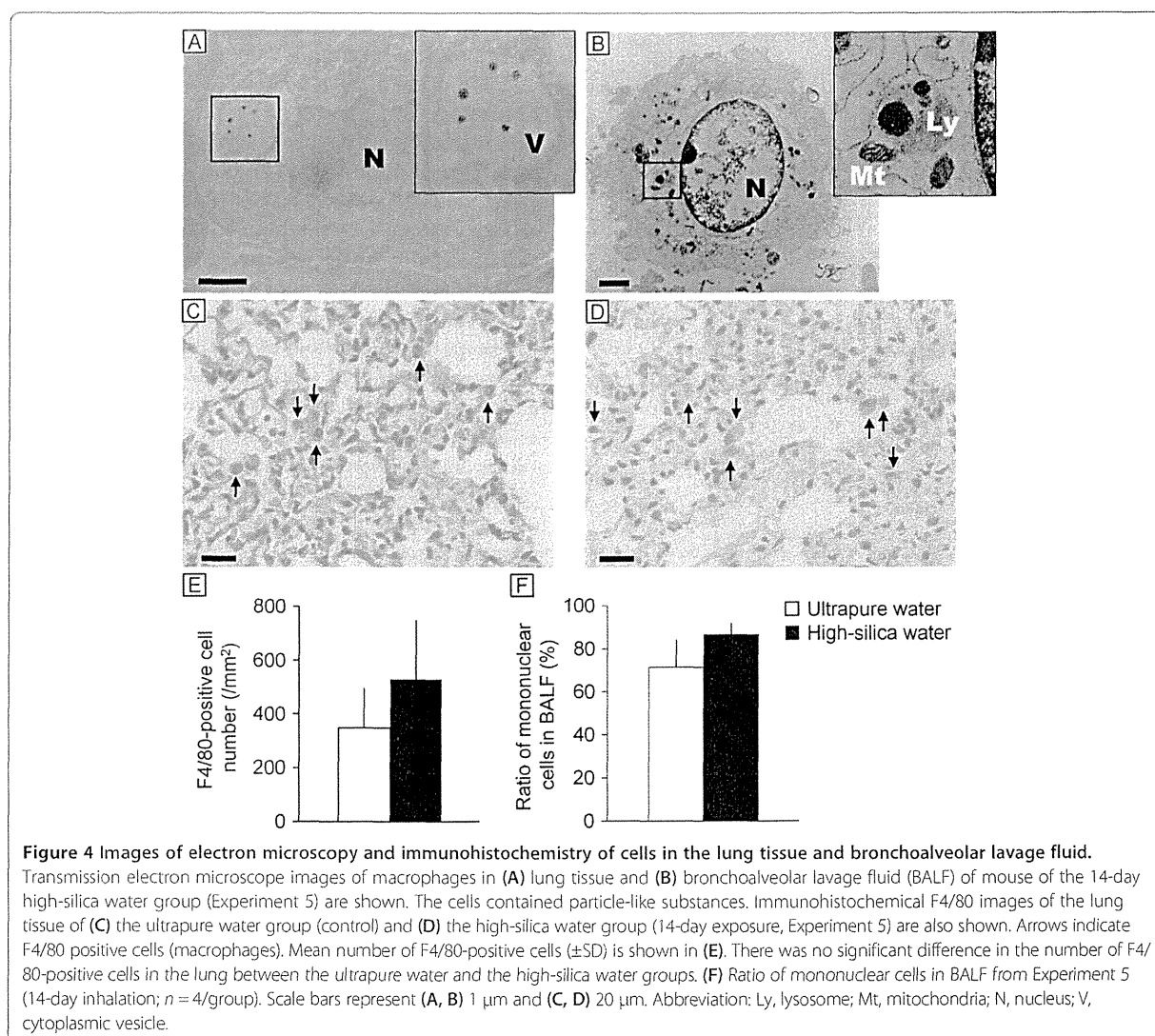

Figure 3 Effect of inhalation of particles released from ultrasonic humidifier on mRNA expression of *Ccl2*, and *Cxcl1* in the lung.
Expression levels of *Ccl2* and *Cxcl1* in the lung tissues (Experiments 3–5, Table 1) were analyzed by an Mx3000P (Agilent Technologies) with SYBR Green Realtime PCR Master Mix (Toyobo). Relative expression levels of the target genes were calculated for each sample after normalization against *Gapdh*. Statistical analysis was performed using an unpaired *t*-test and the level of significance was set at P < 0.05.

Figure 4 Images of electron microscopy and immunohistochemistry of cells in the lung tissue and bronchoalveolar lavage fluid.
Transmission electron microscope images of macrophages in **(A)** lung tissue and **(B)** bronchoalveolar lavage fluid (BALF) of mouse of the 14-day high-silica water group (Experiment 5) are shown. The cells contained particle-like substances. Immunohistochemical F4/80 images of the lung tissue of **(C)** the ultrapure water group (control) and **(D)** the high-silica water group (14-day exposure, Experiment 5) are also shown. Arrows indicate F4/80 positive cells (macrophages). Mean number of F4/80-positive cells (±SD) is shown in **(E)**. There was no significant difference in the number of F4/80-positive cells in the lung between the ultrapure water and the high-silica water groups. **(F)** Ratio of mononuclear cells in BALF from Experiment 5 (14-day inhalation; $n = 4$/group). Scale bars represent **(A, B)** 1 μm and **(C, D)** 20 μm. Abbreviation: Ly, lysosome; Mt, mitochondria; N, nucleus; V, cytoplasmic vesicle.

is much greater than daily $PM_{2.5}$ standard (35 μg/m^3), was also reported when the humidifier was operated in an actual residence environment with tap water containing 303 mg/L TDS [14].

The health effect of airborne particles is one of the main issues in environmental toxicology. The size distribution data on the fog also indicated that it substantially contained submicron-sized particles, which can pass the nasal airways and penetrate down to the lung [24]. Since a case report describing lung injury by "white dust" [15] suggested that the particles from ultrasonic humidifiers may exert adverse effects on the lung, we examined the effects in detail using a mouse model. Although the bacterial contamination was not investigated in the present study, chlorine-disinfected tap water, a commercial mineral water for drinking, and purified water were used for the experiments to minimize the contamination. In general, the

insoluble component of the particles are not dissolved and deposit in pulmonary surfactant, where they are taken up by alveolar macrophages [25,26]. The inhaled particles taken up by the macrophages are transferred to intracellular vesicle and phagolysosome [27], exposed to acidic milieu, and can cause lysosome destabilization leading to inflammation [28]. TEM observation in the present study showed that the particles were being dissolved in the phagosome, and also indicated that the particles generated by the ultrasonic humidifier disintegrated in the phagolysosome of the macrophages. This observation was consistent with our microarray data suggesting that genes dysregulated by the particles from the ultrasonic humidifier were enriched in GO categories associated with MHC molecules and endocytosis. However, expression of *H2-Eb1* was suppressed by inhalation of particles from the humidifier with tap water or high-

silica water. The result was in opposition to the effect of pulmonary exposure (intratracheal instillation) to titanium dioxide nanoparticles [29] and fullerenes [30] on the lung, suggesting that 7- and 14-day inhalation of the particles from the humidifier induced a cellular response from the alveolar macrophages but did not cause acute or sub-acute toxic effects on the lung tissue. This observation was supported by RT-PCR data suggesting that no significant difference in *Ccl2*, *Cxcl1*, and *Tnf* expression between the tap water or high-silica water group and each control (ultrapure water) group. A previous study showed that inhalation of silica-coated nanoparticles (10 mg/m^3; 2 hr/day for 4 days) enhanced *Cxcl1* and *Tnf* expression in mouse lung [23]. Even though the total exposure period in the present study was longer than this previous study, the concentration of airborne particles containing silica from the humidifier was lower. The genes differentially expressed by inhalation of particles from the humidifier were enriched in mitosis, meiosis and related GO and pathways. However, histopathology (including cell proliferation) and macrophage location were not affected by the particles derived from tap water or high-silica water. Our data on the mononuclear cells in BALF indicated that alveolar macrophages tended to be activated by the aerosol particles. The results suggested that 7- and 14-day inhalation of the particles from the humidifier did not cause acute or sub-acute toxic effects on the lung of mice without pre-existing respiratory infection, disease or malfunction.

Conclusion

The present study showed the characteristics of particles generated from ultrasonic humidifiers operated with tap water, a commercial mineral (high-silica) water, and other types of water. This study also showed the effect of 7- and 14-day inhalation of particles released from the humidifier on the lung in a mouse model. The particles were composed of multiple elements including sodium, magnesium, silicate, sulfate, and calcium. Mass and number concentrations and the peak size of the particles were positively correlated to concentration of dissolved mineral components in water provided to the humidifier. Inhalation of particles caused dysregulation of genes related to mitosis, cell adhesion molecules, MHC molecules and endocytosis followed by antigen processing, but did not induce any signs of inflammation or tissue injury in the lung. We conclude that the particles released from the humidifier operated with tap water and commercial mineral water induced a cellular response from the alveolar macrophages but did not cause acute or sub-acute toxic effects on the pulmonary organs in the mouse model. Finally, since the mass concentration of particles generated is linearly correlated with the concentration of dissolved material in water, cautions may be needed to use the

humidifier in some areas with hard water. Long exposure to the aerosol particle from the humidifier may occur in home and working environment. High mineral content tap water is not recommended and de-mineralized water should be recommended in order to exclude any adverse effects.

Additional file

Additional file 1: Table S1. Primer and probe sequences for quantitative RT-PCR. **Figure S1.** Profile of gene expression in the lung *exposed to aerosol released from ultrasonic humidifier with tap water, high-silica water, or ultrapure water.* **Table S2.** Differentially expressed genes with relevant enriched GO and pathways.

Abbreviations
BALF: Bronchoalveolar lavage fluid; cDNA: Complementary DNA; EDS: Energy-dispersive X-ray spectrometer; FE-SEM: Field emission-type scanning electron microscope; GO: Gene ontology; ICP-MS: Inductively coupled plasma mass spectrometry; RO: Reverse osmotic; TDS: Total dissolved solids; TEM: Transmission electron microscope.

Competing interests
The authors declare that they have no competing interests.

Authors' contributions
KT is the main project leader. KT and MU conceived the overall research idea. KSe mainly performed all experiment procedures and data analyses. MU, KSu, MK-I, TI and MS were substantially involved in conducting the experiments and data analyses. MU mainly conducted microarray data analysis. KSu, a specialist in combining nanotechnology and biology, analyzed airborne particles by electron microscopy with KSe. MK-I, an expert on electron microscopy, analyzed particles in the tissue sections with KSe and MU. TI and MS conducted data analyses with pathological and clinical viewpoints. MU and KSe drafted the manuscript. All authors read and approved the final manuscript.

Author details
[1]Department of Hygienic Chemistry, Faculty of Pharmaceutical Sciences, Tokyo University of Science, 2641 Yamazaki, Noda, Chiba 278-8510, Japan. [2]The Center for Environmental Health Science for the Next Generation, Research Institute for Science and Technology, Tokyo University of Science, 2641 Yamazaki, Noda, Chiba 278-8510, Japan. [3]Department of Pathology, Tochigi Institute of Clinical Pathology, 2308-3 Sasayama, Minami-akatsuka, Nogi-machi, Shimotsuga-gun, Tochigi 329-0112, Japan.

References
1. Klepeis NE, Nelson WC, Ott WR, Robinson JP, Tsang AM, Switzer P, Behar JV, Hern SC, Engelmann WH: The National Human Activity Pattern Survey (NHAPS): a resource for assessing exposure to environmental pollutants. *J Expo Anal Environ Epidemiol* 2001, 11:231–252.
2. Norbäck D, Torgén M, Edling C: Volatile organic compounds, respirable dust, and personal factors related to prevalence and incidence of sick building syndrome in primary schools. *Br J Ind Med* 1990, 47:733–741.
3. Harrison J, Pickering CA, Faragher EB, Austwick PK, Little SA, Lawton L: An investigation of the relationship between microbial and particulate indoor air pollution and the sick building syndrome. *Respir Med* 1992, 86:225–235.

4. Carrer P, Maroni M, Alcini D, Cavallo D: Allergens in indoor air: environmental assessment and health effects. *Sci Total Environ* 2001, 270:33–42.
5. Oeder S, Dietrich S, Weichenmeier I, Schober W, Pusch G, Jörres RA, Schierl R, Nowak D, Fromme H, Behrendt H, Buters JT: Toxicity and elemental composition of particulate matter from outdoor and indoor air of elementary schools in Munich, Germany. *Indoor Air* 2012, 22:148–158.
6. Fang L, Wyon DP, Clausen G, Fanger PO: Impact of indoor air temperature and humidity in an office on perceived air quality, SBS symptoms and performance. *Indoor Air* 2004, 14(Suppl):74–81.
7. Melikov AK, Skwarczynski MA, Kaczmarczyk J, Zabecky J: Use of personalized ventilation for improving health, comfort, and performance at high room temperature and humidity. *Indoor Air* 2013, 23:250–263.
8. Environmental protection Agency: *Indoor Air Facts No.8 Use and Care of Home Humidifiers*. 1991. http://www.epa.gov/iaq/pdfs/humidifier_factsheet.pdf.
9. Kane GC, Marx JJ, Prince DS: Hypersensitivity pneumonitis secondary to *Klebsiella oxytoca*, A new cause of humidifier lung. *Chest* 1993, 104:627–629.
10. Suda T, Sato A, Ida M, Gemma H, Hayakawa H, Chida K: Hypersensitivity pneumonitis associated with home ultrasonic humidifiers. *Chest* 1995, 107:711–717.
11. Tyndall LR, Lehman SE, Bowman KE, Milton KD, Barbaree MJ: Home humidifiers as a potential source of exposure to microbial pathogens endotoxins and allergens. *Indoor Air* 2004, 5:171–178.
12. Cheong HK, Ha M, Lee JH: Unrecognized bomb hidden in the babies' room: fetal pulmonary damage related with use of biocide in humidifiers. *Environ Health Toxicol* 2012, 162:e2012001.
13. Rodes C, Smith T, Crouse R, Ramachandran G: Measurements of the size distribution of aerosols produced by ultrasonic humidification. *Aerosol Sci Technol* 1990, 13:220–229.
14. Highsmith VR, Rodes CE, Hardy RJ: Indoor particle concentrations associated with use of tap water in portable humidifiers. *Environ Sci Technol* 1988, 22:1109–1112.
15. Daftary AS, Deterding RR: Inhalational lung injury associated with humidifier "white dust". *Pediatrics* 2011, 127:e509–e512.
16. Brazma A, Hingamp P, Quackenbush J, Sherlock G, Spellman P, Stoeckert C, Aach J, Ansorge W, Ball CA, Causton HC, Gaasterland T, Glenisson P, Holstege FC, Kim IF, Markowitz V, Matese JC, Parkinson H, Robinson A, Sarkans U, Schulze-Kremer S, Stewart J, Taylor R, Vilo J, Vingron M: Minimum information about a microarray experiment (MIAME)-toward standards for microarray data. *Nat Genet* 2001, 29:365–371.
17. Quackenbush J: Computational analysis of microarray data. *Nat Rev Genet* 2001, 2:418–427.
18. Eisen MB, Spellman PT, Brown PO, Botstein D: Cluster analysis and display of genome-wide expression patterns. *Proc Natl Acad Sci USA* 1998, 95:14863–14868.
19. Saldanha AJ: Java treeview–extensible visualization of microarray data. *Bioinformatics* 2004, 20:3246–3248.
20. DATA folder in FTP site of National Center for Biotechnology Information. ftp://ftp.ncbi.nih.gov/gene/DATA/.
21. MSigDB/Download in the GSEA site of Broad Institute. http://www.broadinstitute.org/gsea/downloads.jsp#msigdb.
22. Hung DV, Tong S, Nakano Y, Tanaka F, Hamanaka D, Uchino T: Measurements of particle size distributions produced by humidifiers operating in high humidity storage environments. *Biosyst Eng* 2010, 107:54–60.
23. Rossi EM, Pylkkänen L, Koivisto AJ, Vippola M, Jensen KA, Miettinen M, Sirola K, Nykäsenoja H, Karisola P, Stjernvall T, Vanhala E, Kiilunen M, Pasanen P, Mäkinen M, Hämeri K, Joutsensaari J, Tuomi T, Jokiniemi J, Wolff H, Savolainen K, Matikainen S, Alenius H: Airway exposure to silica-coated TiO_2 nanoparticles induces pulmonary neutrophilia in mice. *Toxicol Sci* 2010, 113:422–433.
24. Oberdörster G, Oberdörster E, Oberdörster J: Nanotoxicology: an emerging discipline evolving from studies of ultrafine particles. *Environ Health Perspect* 2005, 113:823–839.
25. Geiser M, Kreyling WG: Deposition and biokinetics of inhaled nanoparticles. *Part Fibre Toxicol* 2010, 7:2.
26. Scherbart AM, Langer J, Bushmelev A, Van Berlo D, Haberzettl P, Van Schooten FJ, Schmidt AM, Rose CR, Schins RP, Albrecht C: Contrasting macrophage activation by fine and ultrafine titanium dioxide particles is associated with different uptake mechanisms. *Part Fibre Toxicol* 2011, 8:31.
27. Geiser M, Casaulta M, Kupferschmid B, Schulz H, Semmler-Behnke M, Kreyling W: The role of macrophages in the clearance of inhaled ultrafine titanium dioxide particles. *Am J Respir Cell Mol Biol* 2008, 38:371–376.
28. Donaldson K, Schinwald A, Murphy F, Cho WS, Duffin R, Tran L: The biologically effective dose in inhalation nanotoxicology. *Acc Chem Res* 2013, 46:723–732.
29. Park EJ, Yoon J, Choi K, Yi J, Park K: Induction of chronic inflammation in mice treated with titanium dioxide nanoparticles by intratracheal instillation. *Toxicology* 2009, 260:37–46.
30. Park EJ, Kim H, Kim Y, Yi J, Choi K, Park K: Carbon fullerenes (C_{60}s) can induce inflammatory responses in the lung of mice. *Toxicol Appl Pharmacol* 2010, 244:226–233.

Gene Expression Changes in the Olfactory Bulb of Mice Induced by Exposure to Diesel Exhaust Are Dependent on Animal Rearing Environment

Satoshi Yokota[1,2]*, Hiroshi Hori[1], Masakazu Umezawa[2], Natsuko Kubota[2], Rikio Niki[2], Shinya Yanagita[2,3], Ken Takeda[1,2]

1 Department of Hygiene Chemistry, Faculty of Pharmaceutical Sciences, Tokyo University of Science, 2641 Yamazaki, Noda, Chiba, Japan, 2 The Center for Environmental Health Science for the Next Generation, Research Institute for Science and Technology, Tokyo University of Science, 2641 Yamazaki, Noda, Chiba, Japan, 3 Faculty of Science and Technology, Tokyo University of Science, 2641 Yamazaki, Noda, Chiba, Japan

Abstract

There is an emerging concern that particulate air pollution increases the risk of cranial nerve disease onset. Small nanoparticles, mainly derived from diesel exhaust particles reach the olfactory bulb by their nasal depositions. It has been reported that diesel exhaust inhalation causes inflammation of the olfactory bulb and other brain regions. However, these toxicological studies have not evaluated animal rearing environment. We hypothesized that rearing environment can change mice phenotypes and thus might alter toxicological study results. In this study, we exposed mice to diesel exhaust inhalation at 90 μg/m³, 8 hours/day, for 28 consecutive days after rearing in a standard cage or environmental enrichment conditions. Microarray analysis found that expression levels of 112 genes were changed by diesel exhaust inhalation. Functional analysis using Gene Ontology revealed that the dysregulated genes were involved in inflammation and immune response. This result was supported by pathway analysis. Quantitative RT-PCR analysis confirmed 10 genes. Interestingly, background gene expression of the olfactory bulb of mice reared in a standard cage environment was changed by diesel exhaust inhalation, whereas there was no significant effect of diesel exhaust exposure on gene expression levels of mice reared with environmental enrichment. The results indicate for the first time that the effect of diesel exhaust exposure on gene expression of the olfactory bulb was influenced by rearing environment. Rearing environment, such as environmental enrichment, may be an important contributive factor to causation in evaluating still undefined toxic environmental substances such as diesel exhaust.

Introduction

Diesel exhaust (DE) consists of a complex mixture of components in gaseous or particulate form (DEP: diesel exhaust particles). DEP comprise more than 1,000 chemicals that are mainly composed of cores of elemental carbon, traces of metallic compounds, and adsorbed organic materials including polycyclic aromatic hydrocarbons, aldehydes, and nitrogen oxides [1]. DEP accumulate and negatively affect lung function following inhalation exposure. It has been reported that DE causes lung cancer [2], allergic rhinitis [3], and bronchial asthma-like diseases [4]. In fact, the International Agency for Research on Cancer, which is part of the World Health Organization, classified DE as carcinogenic to humans (Group 1) in 2012, based on sufficient evidence that DE exposure is associated with an increased risk of lung cancer [5].

Some research has led to the concern that the brain represents a target for the effects of ambient particulate matter (PM), mainly derived from DEP in urban environments [6]. It has been demonstrated that a small fraction of inhaled nanoparticles may reach the brain [7,8]. Nanoparticles deposit in alveolar and subsequently cross the lung–blood barrier and the blood–brain barrier, and small nanoparticles, especially those below 10 nm, deposit efficiently on the olfactory mucosa by diffusion. Subsequent uptake and translocation of nanoparticles along axons of olfactory nerves has been reported [9,10]. Previous in vitro studies have demonstrated that nanoparticles, such as DEP, might cause neurotoxic effects and disturb blood–brain barrier function [11,12]. In addition, in vivo studies also have demonstrated that DE inhalation exposure has inflammatory effects on the olfactory bulb and midbrain regions of the brain [13,14].

However, these toxicological studies have not evaluated the effects of conditions in the animal rearing environment. Effects of exposure to environmental chemicals and materials including nanoparticles are usually assessed in a standard laboratory cage environment alone. Mice housed in standard laboratory cages demonstrate frequent stereotyped behavior, in particular sponta-